Master Erasmus Mundus in
Color in Informatics and Media Technology (CIMET)

Robust Iris Recognition Using Light-field Camera

Master Thesis Report

Presented by

Kiran Bylappa Raja

and defended at

Gjøvik University College

17th June, 2013

Academic Supervisor(s): Dr. Raghavendra Ramachandra
Assoc Prof. Faouzi Alaya Cheikh
Prof. Christoph Busch

Jury Committee: Assoc Prof. Éric Dinet
Assoc Prof. Juan Luis Nieves Gómez

Robust Iris Recognition Using Light-field Camera

Kiran Bylappa Raja

2013/06/17

Contents

Abstract

With the growing concern for security, it becomes necessary to identify a subject or verify a subject against many other subjects. Both of these methods demand high amount of accuracy for application in security. Human physical features based biometrics have been popular choice in biometric applications owing to the ease of extracting biometric features like face, fingerprint, iris from a subject. Iris is a robust modality as compared to face or fingerprint in identifying a subject due to high amount of texture information present in it. Because of its robustness in verification/identification, iris recognition has gained significant interest from both the industry and academia. Even with the advances in iris recognition domain, low quality images due to out-of-focus issue in iris imaging is predominant with conventional iris imaging systems. We propose a novel scheme to capture high quality iris samples by exploring new sensors based on light-field technology. The idea stems out from the availability of multiple depth/focus images in single exposure and the possibility of using them to obtain an all-in-focus image from new and emergent light-field imaging technology. The proposed scheme has been experimentally verified with a unique and newly acquired iris database. The results suggest promising future in application of the proposed scheme in real-life verification/identification scenarios.

Summary

Considering the success factor of the biometrics over traditional authentication methods, many organizations have employed biometric systems for secure authentication. With the challenges growing at par with the improvements in biometrics, it is essential to provide convenience to genuine subjects while preventing the imposters. The accuracy of iris recognition system has influenced biometric systems' accuracy in large scale. Although iris recognition systems provide high accuracy in verification/identification of subjects, low quality images due to out-of-focus iris imaging continues to impact the performance.

With the advent of new generation of imaging sensors based on light-field technology, it is possible to exploit the multiple depth/focus images to obtain a best focused image. Employing the best focus iris image guarantees high amount of iris feature information for verification/identification. With the goal of addressing out-of-focus iris imaging, a new approach to the problem is proposed in this thesis. The first generation of consumer light-field cameras is employed to demonstrate the cost-effectiveness of the proposed scheme.

This thesis is structured as follows: A brief history of light-field imaging is presented in Chapter 2. Chapter 3 gives the description of necessity for iris recognition and a review of the state-of-the-art. Chapter 4 presents the arguments as to why it is of significant interest to employ light-field technology in iris imaging. Two new iris databases are presented in Chapter 5 and an experimental dissertation is put forward in Chapter 6. A detailed analysis of the obtained results and its impact on the future of iris recognition systems is available in Chapter 7.

Appendix A contains the extended set of experiments and the results obtained. Appendix B presents the scientific paper disclosing the results of experiments for iris recognition in visible spectrum using light-field cameras. This paper has been accepted for publication in CVCS2013 (IEEE conference proceedings) to be held at Gjøvik, Norway in September 2013.

List of Figures

List of Tables

1 Introduction

1.1 Motivation

Identification is increasingly becoming necessary for secure movements and applications. Many approaches exist for identification which include biometric signatures, secure codes, passwords among many other. In case of identification using secure codes or passwords, the identity can be lost, stolen, shared or manipulated and thereby introduces the risk in intended security. This has lead the research to a whole new direction to explore the biometric signatures. Unlike secure codes or passwords, biometric signatures do not need to be remembered and they are never at the stake of misuse. Thus biometric signatures increase the level of accuracy in security.

Most common forms of biometric systems include either physical characteristics like face, fingerprint, iris, vein pattern or behavioural characteristics like gait, keystroke dynamics. Due to the uniqueness and the high amount of distinct information in the iris pattern, iris recognition has drawn substantial amount of interest in the biometric research community. Additionally, iris recognition has been proven to be a robust modality with reliable performance for human subject verification.

As with any other biometric verification systems, iris recognition presents some open challenges. Even after considerable amount of work, iris recognition in visible spectrum has remained with issues such as out-of-focus iris capture and lower rate of iris recognition for darker iris. The initial goal of this work is to address the problem of out-of-focus iris image capture predominantly present in the current iris recognition systems in visible spectrum.

1.2 Research Questions

Although there exist a number of challenges, this work focuses on deriving a novel way to address the problem of out-of-focus in visible spectrum iris imaging systems. The goal of this work is also to propose a simple yet efficient scheme with viable cost to solve the out-of-focus iris imaging in the visible spectrum. After the detailed study of the existing works, more concrete research questions have evolved. The main questions answered in this work are:

1. Can the out-of-focus imaging present in visible spectrum iris recognition systems be addressed?
2. Can we adopt the existing imaging system to solve the issue of out-of-focus by extending the Depth-of-Field(DOF)?

1.3 Structure Of Dissertation

This thesis consists of three major sections:

1. An introduction to light-field technology : Chapter 2 gives a brief history and an

introduction to the light-field technology.

2. State-of-the-art in iris recognition : Chapter 3 gives an introduction to biometrics and specially, iris recognition. It also discusses the existing schemes in iris recognition systems and exemplifies the challenges for iris recognition systems in visible spectrum.
3. Contribution of the work : Chapter 4 proposes our approach to address out-of-focus in iris imaging. Chapter 5 presents the databases constructed during the course of this work and Chapter 6 details the results obtained for the conducted experiments and the discussion on the results obtained. Chapter 7 draws the conclusive remarks of this work and presents the foreseeable research opportunities in this direction.

2 Light-field Imaging

A 2D image is formed by combining the intensity of light falling on photosensor. Thus the image captured using conventional camera can place a nice 2D scene in focus and view with fixed aperture. While in light field imaging, the 4D radiance is captured of which 2 dimensions correspond to the view of the scene and the other 2 dimensions to angular information of the scene. Thus, the 4D light-field is nothing but the radiance along rays in empty space. A light field can be interpreted as all possible information captured from the camera's field of view that result in a 2D collection of 2D images of a scene and hence, a 4D array of pixels [1]. This chapter, discusses the fundamentals of light-field or plenoptic imaging in brief.

2.1 Plenoptic Function

Adelson and Bergen [2] demonstrated that all the basic visual measurements can be considered to characterize local change along one or more dimensions of a single function and this function described the structure of the information in the light observed by any observer. As this function describes all possible information from the scene, they called it a *Plenoptic function* [1]. Any gray-scale pin-hole camera records the intensity distribution P which can be parameterized as $P(\theta, \phi)$ in spherical co-ordinates. Extending it to color camera, the intensity distribution P can be modified to accommodate the wavelength λ. The new intensity distribution thus becomes $P(\theta, \phi, \lambda)$. A set of images in a continuous time is a movie. Thus the intensity distribution P of movie can be extended as intensity distribution $P(\theta, \phi, \lambda, t)$. If P is varied with respect to viewing position V_x, V_y & V_z we obtain P, which is traditionally called *Plenoptic function* that can be written as :

$$P = P(\theta, \phi, \lambda, t, V_x, V_y, V_z) \tag{2.1}$$

For a given wavelength, a given time, and a given viewing position in space, there exists a pencil of light rays passing through the viewing point [2]. The collection of all the rays constitutes a *light-field image*. The plenoptic function describes the intensity of each light ray in the real world as a function of the seven parameters listed above.

2.2 Plenoptic Camera

All the rays passing through the lens of the camera are recorded on the sensor. These recorded values are the average values of the all the rays converging at a particular location on the sensor regardless of the angle of incidence of incoming rays. The camera which is able to capture a chunk of optical structure of light impinging on lens and record the appearance of the world from all possible viewpoints within the available lens aperture is called *'Plenoptic camera'* [3]. Thus, the plenoptic camera captures the scene as the continuum of viewpoints that lie within the aperture of the main camera lens.

[1] Plenus, means complete or full. The optic function describing everything is called Plenoptic.

Adelson and Wang [3], designed a plenoptic camera using a lenticular[2] array to retain the structure of light impinging on the sensor array. They used image processing techniques to obtain the simulated images based on the viewing position. This camera construction technique was used to measure the parallax corresponding to virtual displacements in viewing positions. The whole procedure is illustrated in Figure 1 .

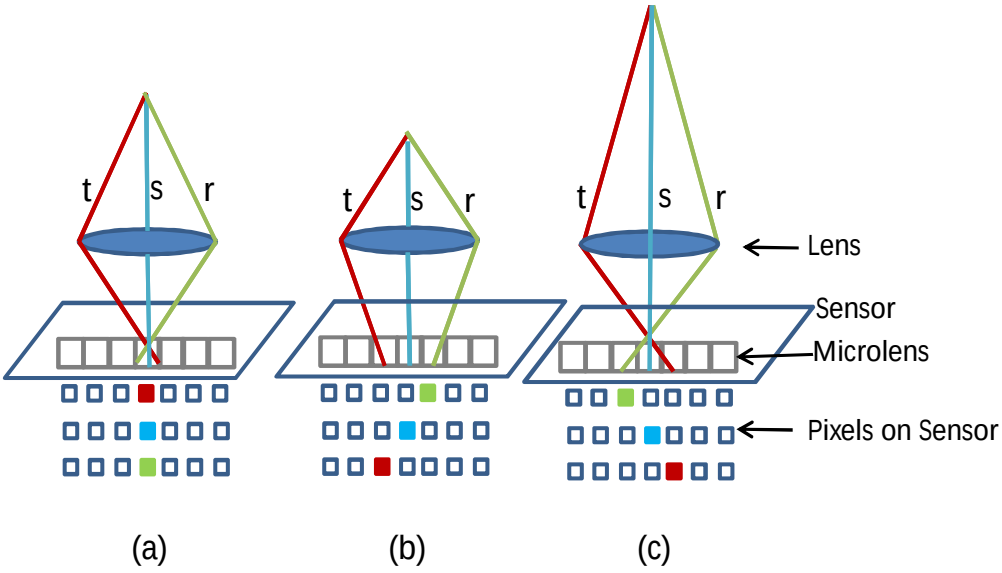

Figure 1: Light-field structure analysis; (a), (b) and (c) show different ways of light ray collection on sensor when passing through microlens (inspired from Adelson and Wang[3]).

Each impinging ray of light is broken into three sub-parts corresponding to their angle of incidence. The sub-pixels are identified as *r, s* and *t* corresponding to right side, center and left side of lens respectively. The image formed by all *r* pixels over the sensor corresponds to the scene viewed on the right side of the camera lens/sensor. Similar argument holds good for images formed by *s* and *t*. The new convention of *macropixel* arose out of this design and it consisted of a set of pixels on image sensor which corresponds to one point in the real world. In the case of above illustration, *r, s* and *t* constitute a *macropixel*.

It has to be noted that the spatial resolution of the effective image is reduced by a factor corresponding to subpixels in a *macropixel* along the horizontal and vertical direction. If the effective size of sensor is $x*y$ (corresponding to horizontal & vertical direction) and each *macropixel* consists of $m*n$ pixels (corresponding to horizontal & vertical direction), then the effective image resolution is decreased by a factor of $m*n$.

2.3 Light-field Rendering

McMillan and Bishop [4] used the plenoptic function as a parameterized function to describe the scene from a given point in space. They reduced the 7 dimensional function given by Adelson and Bergen [2] in Equation (2.1) to a 5 dimensional function ignoring

[2] Lenticular refers to a sheet of lens consisting of an array of optical elements called lenticules that create a convex perspective of multiple images. Source : `http://www.rays3d.net/about-lenticular.html`

[3] Source : Adelson, E.H. and Wang, J.Y.A., Single lens stereo with a plenoptic camera[3]

the wavelength (λ) and adopting a constant time instance *t*. McMillan and Bishop [4] represented 5D light-fields as a set of panoramic images captured at different 3D world locations. The modified *plenoptic* function can be written as:

$$P = P(\theta, \phi, V_x, V_y, V_z) \qquad \text{for a constant time } t \tag{2.2}$$

Levoy and Hanrahan [5] proposed a method of interpreting the input images as slices of 2D within a 4D light-field function. The image captured on a sensor is nothing but the radiance as a function of position and direction ignoring the occluded regions in the scene being captured. Unlike the method proposed by Adelson and Bergen [2], Levoy and Hanrahan [5] considered the light-field as a 4D function further reducing the proposed equation by McMillan and Bishop [4]. Levoy and Hanrahan [5] postulated that the radiance does not change along a line provided the region is occlusion free and capturing this data would just have the redundant data, leading to a increased data size and complex reconstruction techniques.

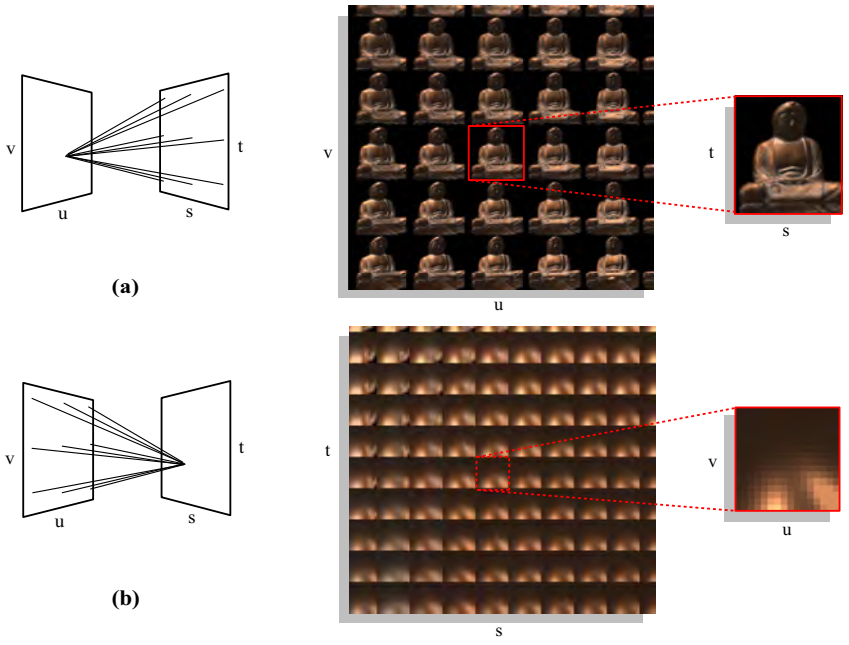

Figure 2: Levoy's illustration of light-field resampling; Two visualizations of a light-field. (a) Each image is the representation of the rays arriving at one point on the (u,v) plane from all points on the (s, t) plane. (b) Each image is the representation of the rays leaving one point on the (s, t) plane for all points on (u, v) plane.
(Image credit : Levoy, M. and Hanrahan, P.[4])

A new image is then generated by combining different parts of the light-field image with a simple process of linear resampling. Levoy and Hanrahan [5] parameterized the

[4]Source : Levoy, M. and Hanrahan, P., Light field rendering[5]

lines by their intersection with planes in arbitrary position and they defined the first plane as (*u,v*) and second as (*s,t*). Light-field can be visualized in two ways :

1. The projection of lines emerging from *(u, v)* plane onto *(s, t)*.
2. The projection of lines emerging from *(s, t)* plane onto *(u, v)*.

The first approach is non-sheared view and the latter approach is termed as *sheared* perspective view of scene *off-axis*. It can be noted that both the planes are consisting of the recorded incoming light rays corresponding to the scene being captured. As illustrated in Figure 2, the image coordinates from (*x, y*) plane can be transformed to (*u, v*) and (*s, t*) using a projective map transformation. Figure 2(a) shows the sheared perspective views of scene, while the Figure 2(b) shows the non-sheared view.

The image captured on the (*x, y*) plane is the set of the all the light rays passing through the light-slab planes (*u, v*) and (*s, t*). In effect, the combination of planes (*u, v*) and (*s, t*) works as a *Ray Filter* as shown in Figure 3. The anti-aliased image for all the possible viewing angles of the sensor is obtained through the method of 4D re-sampling. It is also recommended to filter the data on sensor using 4D low pass filter. They also propagated the idea of averaging multiple views in light-field to obtain a synthetic aperture image under coherent illumination.

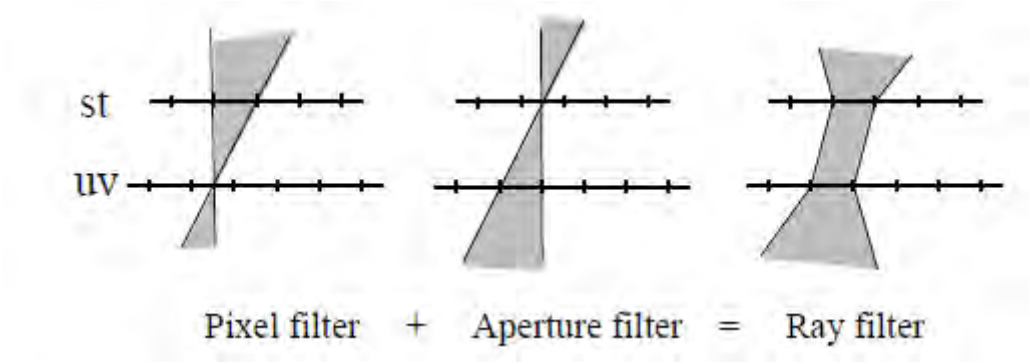

Figure 3: Light-field image as ray filtered image
(Image credit : Levoy and Hanrahan[5])

Unlike the approaches mentioned previously which use multiple exposure, Ng et al. [6] proposed a camera which sampled the 4D light field on sensor in single photographic exposure. They employed depth of field camera with an additional microlens array inserted between the camera sensor and the main lens. In their work, Ng et al [6] captured the scenes with a large lens aperture and recomputed the image using sharper focus at different depth based on the sensor data.

The basic principle propagated by Adelson and Wang [3] was extended to the handheld camera by placing the microlens array to augment the 2D photosensor. The images were first demosaiced and then the lateral misalignment was corrected by rotation, interpolation and integration of number of pixels in microarray.

[5]Source : Levoy, M. and Hanrahan, P., Light field rendering[5]

Vaish et al. [7] represented the light-field using plane and parallax in combination with synthetic aperture photography techniques to obtain the occluded objects partially with different levels of sharpness in the image. Isaksen et al. [8] showed the use of wide aperture to view occluded objects. Favaro et al. [9] used finite aperture of single camera lens to reconstruct the partially occluded objects.

Fife et al. [10], demonstrated a prototype of single-chip multi-aperture image sensor which could capture high resolution 2D image and 3D depth map of the scene. The $m \times n$ sized sensor consisted of local optics corresponding to $k \times k$ pixel array. The image is focused above sensor plane to obtain partially overlapping images through the local optics. This method of imaging achieves higher spatial resolution compared to traditional plenoptic camera prototype proposed by Adelson and Wang [3] and depth is extracted by disparity of apertures.

Inspired by the idea of Ng et al. [6], Veeraraghavan et al. [11] developed a novel method and termed it as *'Dappled Photography'*. They used printed high frequency sinusoidal masks in front of the camera sensor and captured the light coming from the objective lens. They employed a reconstruction method based on heterodyning in frequency domain. They also proposed a camera design based on broadband mask in lens aperture. Both of these techniques minimized the loss of spatial resolution.

Instead of using a plenoptic lens arrangement, Liang et al. [12] used different coded apertures in front of the lens to obtain the angular information. Angular resolution was traded off for the spatial resolution in this case. Set of images obtained using various coded apertures gave the scene capture at different depths. For each light-field image, the feature points are extracted and interactively refocused using region of interest followed by removal of outliers. The images are then shifted and added together to generate the in-focus image.

2.4 Commercial Light-field Cameras

Recent interests in the light-field imaging has resulted in two commercially available devices. One of the device is from Raytrix GmBH [13] and the other is from Lytro Inc. [14].

2.4.1 Lytro Light-field Camera

Lytro Inc. [14] has rolled out the first commercial and consumer oriented light-field camera with 11 Mega Rays. With the main optical lens at f/4 and 100000 micro-lenses focused at infinity, Lytro light-field camera provides an effective spatial resolution of 1.2 MP. Lytro light-field camera is a low cost device, portable and user friendly.

Figure 4: Lytro light-field camera
(Image credit : Lytro Inc[14])

2.4.2 Raytrix Light-field Camera

Raytric GmBH [13] has introduced first generation of industrial quality light-field cameras. The lowest available configuration from Raytrix has 20000 micro-lenses and 11 Mega Rays providing an effective spatial resolution of 2.7 Megapixels. Unlike the microlenses in Lytro light-field camera which are focused at infinity, each of the microlens in the Raytrix light-field camera is focused differently. Further, Raytrix also supports video rendering at 6 frames/sec even with the low-end light-field cameras. On the downside, these cameras are high in cost and computationally more expensive.

Figure 5: Raytrix R11 light-field camera
(Image credit : Raytrix GmBH[13])

2.5 Light-field Imaging And Conventional Imaging

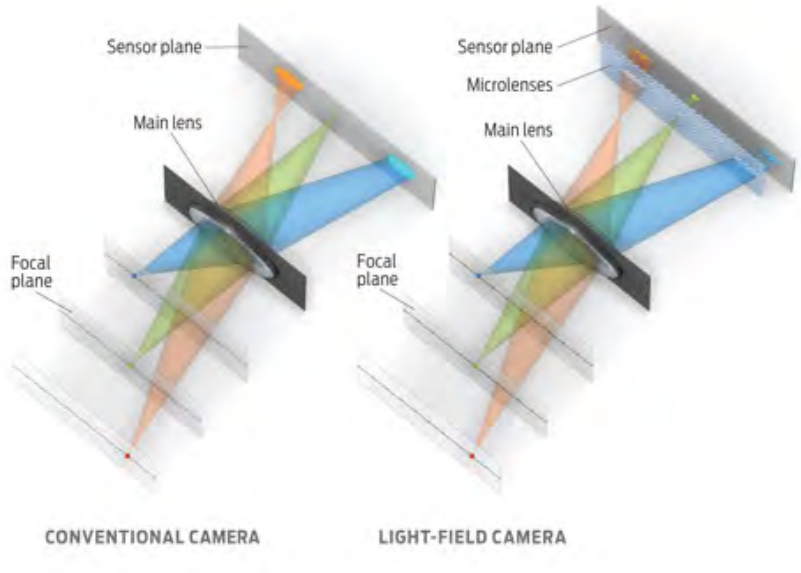

Figure 6: Light-field camera working principle (Image credit : Emily Cooper[6])

Figure 6 illustrates the working of the light-field camera. On the left hand side of the figure, the working of the conventional camera is shown and the right side of the figure gives the details of light-field camera. In case of conventional sensor, the image is at right-focus for one particular focal plane. In the light-field camera employed in our work, a micro-lens array is inserted in between the optical lens set and the sensor. The collected information from different focal plane is resampled dynamically to generate images corresponding to different focal planes. The final image obtained in a conventional sensor corresponds to sharpest image for the green optical path. The images related to orange and blue optical path is not in focus. In light-field sensor, the scene data from blue, green and orange paths are collected on the micro-lens array before they are collected on the sensor, thereby capturing scenes in different focal planes, thus scenes at different focal planes can be reconstructed.

2.6 Discussion

Of all the different methods of generating light-field images, in this work, we have used the implementation work of Ng et al. [6]. The research output by Ng et al. [6] has been adopted in the development of the Lytro light-field camera [14] which is commercially available . The portability of the device and ease of handling coupled with high shutter speed and low cost has motivated us to employ the camera in our work.

[6]Source : Harris, M. 2012. Focusing on everything.[15]

3 Iris Recognition In Biometrics

3.1 Biometrics

The term biometrics recognition refers to "automated recognition of individuals based on their behavioural or biological characteristics" [16]. Fingerprints, iris, face, hand and voice are some of the well known biometric features which can be used for the verification or identification of individuals by comparing the acquired biometric feature against the stored biometric feature. Biometric recognition is known to be robust compared to rest of the methodologies of subject identification or verification owing to its uniqueness for each individual subjects. The available biometric signatures can be divided as:

1. **Physiological Biometrics**: Based on the physical features like face, fingerprint, iris, vein of human body.
2. **Behavioral Biometrics**: Biometric recognition based on the behavioral characteristics of the subjects/persons. Speech, gait and keystroke based biometrics can be exemplified for this category.

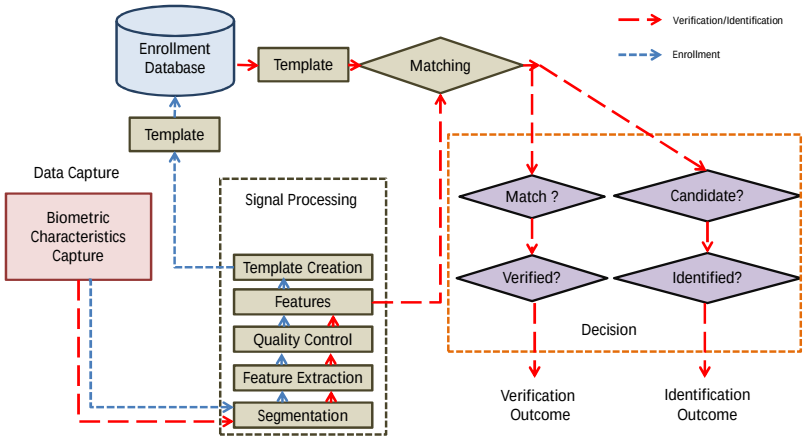

Figure 7: General biometric system (Simplified illustration inspired from [16])

Figure 7 shows the general architecture of any biometric system. Biometric system typically has data capture system, signal processing system, data storage system, matching and decision making system. The biometric samples for any subject are captured using various sensors in data capture system which is processed in the signal processing unit. The biometric samples are segmented and the features are extracted. The extracted features are accepted or rejected based on the predefined quality criteria. The samples passing the quality criteria are stored as templates in the enrolment database. The stored templates are used for comparison to verify or identify a subject.

Approaches involving more than one biometric signatures are also used to address or

overcome the issue of ambiguity as multiple sources provide the supplementary information for biometric recognition. In this work, we primarily concentrate on the physiological biometrics and investigate the robustness of iris recognition in visible spectrum for the images captured through a new generation of sensors called as Light-Field Cameras. As a primary stage of investigation, we have conducted the experiments in visible spectrum using the first generation of consumer light-field cameras by Lytro Inc. [14].

3.2 Iris Recognition

Human iris is one of the most distinctive features for an individual and is thus used for the robust biometric recognition. Owing to the robust level of identity protection it provides, iris recognition is unparalleled by any other biometric features. Iris biometric feature is not prone to the vast changes or morphing over the period of lifetime.

The human iris is defined as a thin circular diaphragm lying between the cornea and the lens in eye [17]. Iris is one of the organs present internally in human body but also visible externally when the eye-lids are open. The iris is known to develop in the third month of gestation and its prominent structures resulting in the patterns are mostly complete by eighth month [18]. It contains rich amount of texture along and unique structures like furrows, freckles, crypts, and coronas [17]. Figure 8 shows a sample eye image illustrating various parts. Color of the iris is known to vary individually for each person. The color is related to density of melanin pigment in the anterior layer and stroma [19] in iris. The presence of lower amount of melanin pigment in iris results in light colored iris and the higher amount results in darker iris. Light colored iris allows the penetration of long-wavelength light and usually scatters shorter wavelength light [19]. In general case of lighter iris, visible spectrum can be used to capture the image. But in the case of darker iris, the state-of-the-art systems use Near Infra Red (NIR) wavelength light to capture the pattern of high amount of texture.

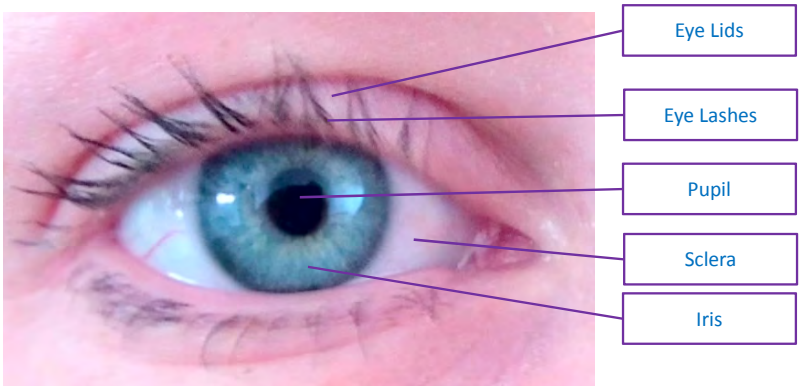

Figure 8: Parts of the human eye

Previous works by Daugman [20] have reinstated the stability of this biometric feature over a long period of lifetime. Owing to its stability and uniqueness to each individual, it

is well known and preferred biometric characteristic. Iris is not at the risk of changes due to external factors as in the case of face or fingerprint [20, 21]. Iris recognition is deemed to be less error prone, robust to changes with growing age and less likely to be morphed intentionally as it involves surgical change of eye balls. To the best of our knowledge, there are no studies which detail the specificity of the changes in patterns inside the iris with respect to the age of any individuals. Due to planar nature of iris, it does not have much sensitivity to angle of illumination and any minor affine transformations caused due to change in viewing angle is easily corrected [20]. Daugman [20] has also developed the methods to reverse the pattern distortion due to dilation of pupils in the eyes. All these factors make iris recognition more preferred than other biometric modalities.

One important aspect to consider is epigenetic nature of iris patterns. This results in unique, completely independent and uncorrelated iris patterns for an individual and also for identical twins. Biometric features such as face or fingerprint are always at the risk of being changed due to various factors. The performance of the recognition system depends largely on the change in facial expressions based on the social factors and also throws challenges in recognition with varied illumination, age, and pose [22]. Another well known biometric modality is fingerprint. Any intentional or unintentional scars or cuts on the fingerprint may introduce false recognition or reject the authentic subjects. Fake fingerprint attacks has to be considered for a secure biometric recognition. These factors influence the intra-class variability to larger extent and thereby make the inter-class variability lower. Lower inter-class variability leads to challenges in accurate recognition. Thus, iris provides two unique biometric identity for any single person with a high level of identification confidence.

One of the key large scale projects like UIDAI [23], where the biometric identity of each individual is enrolled, intends to collect the iris data also. The standards committee at UIDAI [23], opine that iris can provide accuracy in large scale biometric recognition. UIDAI also intends to fuse the scores of two uncorrelated modalities such as face or fingerprint to provide better accuracy than any single modality to reduce risk of imposter feature match in order to achieve the foreseen target accuracy [24].

3.3 Visible Spectrum Iris Recognition

Atos Origin [25] has reported that stop-and-stare strategy followed by many iris recognition systems to acquire good quality images in the Near-Infra-Red region ($700-900\mathrm{nm}$) remains a major hurdle in deploying the iris-based biometrics in large scale. Many of the currently deployed systems impose constraints on the subjects and acquisition environment. A subject is expected to stand close to the imaging device and co-operatively look into the near-infra-red (NIR) camera to assure good quality images. To achieve a good signal-to-noise ratio in the sensor and to capture images with highly discriminating iris features with reasonable contrast, high illumination is required [26]. This becomes non-acceptable for acquisitions under at-a-distance scenario because of amount of light required for the process. Darker iris needs much higher illumination for capturing the texture information. But the reported standards from American and European standards council limits the irradiance in NIR illumination to $10\mathrm{m}W/\mathrm{cm}^2$ [26].

Contactless capture of human iris resembles more of the real-life scenario and thus aids in acquiring the iris without the knowledge of subject being imaged. This kind of imaging also aids in obtaining iris-on-the-move and thereby, relaxes the constraints posed by the NIR acquisition. It should also be noted that the ease of capture comes with quite many challenges like noise in the imaging, specular reflections, shadow, out-of-focus images which impact segmentation and thus recognition accuracy. The conventional iris imaging sensors exhibit the limitations of fixed point of view and thus the focus remains constant during the acquisition. With no methods to achieve high sharpness from the captured image, in this work, we have explored the iris recognition in visible spectrum and have addressed the issue of bad quality images due to out-of-focus imaging using light-field camera which support focusing after the capture.

3.4 State-of-the-art In Iris Recognition

This section discusses the complete pipeline involved in near-infra-red iris recognition which also holds good for visible spectrum iris recognition. Details of the existing state-of-the-art and key techniques involved in this work are discussed.

3.4.1 Segmentation

The prime task in any iris recognition system is to segment the iris region from the captured eye image. In a broader perspective, iris region is segmented by estimating the region between two ellipses or circles. Two ellipses or circle boundaries are constituted by the regions between pupil-iris and iris-sclera. This section provides the details on the existing methods for segmenting the iris from the eye image. It also gives the detailed description of the segmentation approach used in our work.

Efficient segmentation of the iris image influences the biometric recognition largely. It depends on the quality of the image and the contrast difference between the pupil-iris of image. In any of the naturally illuminated acquisition conditions for eye images, the resulting images might contain considerable amount of specular reflections. It becomes essential to mitigate specular reflections for obtaining the clear segmentation of iris pattern.

The strategies of iris segmentation can be classified as: "Contour First" and "Texture First" [27]. In *Contour First* method, the pupil is roughly localized and then the iris boundary regions are estimated to localize the iris texture whereas in *Texture First* method, iris texture is localized following the initial guess of the pupil. Hough transform based approaches can be exemplified for *Contour First* strategy and techniques used in OSIRIS [28] belong to *Texture First* category.

3.4.1.1 Hough Transform Based Approaches

The simplest approach of detecting the iris and pupil boundary is based on Hough transform [29]. Modified version of the Hough transform is generally adopted to detect the circles in an image. The edge map information is projected into Hough space and the parameters of circles passing through each edge point are detected. This information is inturn used to detect the centre of the circle. The equation for the circle in Hough space is:

$$(x - x_o)^2 + (y - y_o)^2 = r^2 \tag{3.1}$$

where, x_o and y_o represent the center of the circle with the radius r.

Wildes et al. [30] used the information from directional filters to estimate the boundaries of eyelids and thereby having a better estimate of the iris boundary with lesser distortion. Kong et al. [31] used a similar approach of detecting the upper and lower eyelids using the parabolic Hough transform. Other well known works based on Hough transform include the work of Tisse et al. [32]. Although this method has proven useful for the iris segmentation in the NIR image acquisition, due to the very low contrast difference between iris and pupil boundary in the visible spectrum, it does not allow to set an uniform threshold for detecting the edges and thus produces unstable segmentation output in visible spectrum. It has to be noted that this method is also not robust against specular reflections.

3.4.1.2 Integro Differential Operator

Daugman [33] used integro differential operator for segmenting the iris from eye image. The integro differential operator located the circular iris, pupil regions and the eyelids. Basically it can be considered as modified version of Hough transform owing to its similarities of finding the first derivatives of the image to estimate the geometric parameters for detecting the iris-pupil boundary. The method of integro differential operator does not necessarily depend on thresholding to detect the circles mainly because the estimation is purely based on the image derivatives. Although the method is good, it fails to take care of the glare/reflections and thus arises the need for high quality images in the close range capture with almost no reflections.

Daugman's integro-differential operator is given by :

$$\max_{(r,x_o,y_o)} \left| G_\sigma(r) * \frac{d}{dr} \oint_{(r,x_o,y_o)} \frac{I(x,y)}{2\pi r} ds \right| \tag{3.2}$$

where $I(x,y)$ is the image of the eye, r is the search radius, $G_\sigma(r)$ is Gaussian smoothing function, and s is the contour of the circle given by the coordinates (r, x_o, y_0).

The integro-differential operator searches for the maximum in the blurred partial derivative and by increasing radius r. The integro-differential operator is a circular edge detector, blurred at a scale set by σ and searches maximum contour integral derivative iteratively with the help of (r, x_o, y_0).

3.4.1.3 Segmentation Frameworks

With the availability of different approaches to segment the iris images, two popular standard segmentation benchmarks are Masek's [34] implementation based on Hough transform and OSIRIS (Open Source for IRIS) [35] based on Daugman's works. Masek's method is adopted as a standard by NIST and OSIRIS is reported to outperform Masek's method in-terms of the segmentation accuracy [35]. Both of the methods are available publicly. In this work, we have used OSIRIS software to segment the iris images based on the reported accuracy and its robust segmentation [35].

3.4.1.4 OSIRIS : Segmentation

The previous works by Daugman [36] and Pundlik et al.[37] have considered non-circular parametric contours for iris normalization for pupil with large dilation. Hollingsworth

et al. [38] have indicated the necessity to not just use the circular approximation for localizing the iris and pupil boundaries. OSIRIS [28] based segmentation finds more accurate contours of iris by clearly distinguishing the inner boundary between pupil/iris and outer boundary between iris/sclera. This results in classifying the image into iris and non-iris parts.

With the a-priori estimate of pupil radius r, the center of the pupil region is searched. The minimum from the image corresponding to image filtered by a disk-shaped kernel of size $r \times r$ with radius r such as the one shown in Figure 9 is searched. It can be considered a summation over the disk-shaped neighborhood. The exact pupil is located by normalizing the result of filter in the range of 0 to 1. A pixel is considered a pupil candidate if the inverted value is 0.

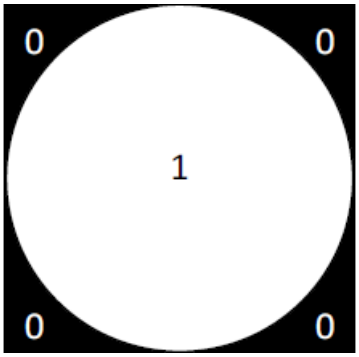

Figure 9: Pupil detection kernel; Source : "http://svnext.it-sudparis.eu/svnview2-eph/ref_syst//Iris_Osiris_v4.1/doc/"

The two key criteria for estimating the pupil are:

1. A disk-shaped neighbourhood kernel of radius r is used to estimate the pixel as a candidate for pupil. If the summed value inside this kernel is close to 0, the corresponding pixels are considered to constitute the pupil.
2. The angle between the gradient at point P, $\overrightarrow{G_P}$ with the aligned line formed by center of the pupil O and point P should be 0 or close to 0 [28]. Steps involved in this can be summarized as:
    1. Computing horizontal and vertical Sobel gradient maps, X_{G_P} and Y_{G_P} for the image.
    2. Building kernels of size $r \times r$: X_{OP} and Y_{OP} .
    3. Filtering gradient X_{G_P} by X_{OP} and Y_{G_P} by Y_{OP}.
    4. Finding location of maximum of the two filters.

$$\frac{1}{N}\sum_{p=1}^{N} Cos\theta_p = 1 \qquad \text{since } \theta_p = 0 \tag{3.3}$$

$$\frac{1}{N}\sum_{p=1}^{N} \frac{\overrightarrow{G_p} \bullet \overrightarrow{OP}}{\left\|\overrightarrow{G_p}\right\| \bullet \left\|\overrightarrow{OP}\right\|} = 1 \qquad \text{using the scalar product} \tag{3.4}$$

$$\frac{1}{N}\sum_{p=1}^{N} (X_{G_p}.X_{OP} + Y_{G_p}.Y_{OP}) = 1 \qquad \text{assuming unit vectors} \tag{3.5}$$

where N is the number of points in kernel neighborhood. Equation 3.5 boils down to sum of two filtering operations in horizontal and vertical direction. X_{OP} and Y_{OP} can be written as:

$$X_{OP} = \frac{x}{\sqrt{x^2 + y^2}} \tag{3.6}$$

$$Y_{OP} = \frac{y}{\sqrt{x^2 + y^2}} \tag{3.7}$$

where x and y are the coordinates of point P relatively to center O. For further details on the method, the reader is referred to the "Biometric Reference System" [28].

3.4.1.5 Iris Localization

Anisotropic smoothing is applied on the gradient map of the image. The resulting image is processed using Viterbi algorithm. To find the exact contours, Viterbi algorithm is applied on the high resolution image. Also, to determine the coarse edges, low resolution image is processed. This helps in determining more accurate circles [39].

OSIRIS also generates the mask corresponding to the detected iris as in Masek's implementation. The output of the segmentation is used in the normalisation. The details of normalisation techniques are described in the next section.

3.4.2 Iris Normalization

To perform the comparisons of iris, it is essential to convert the segmented iris into a uniform scale image with fixed dimension. The shape of the pupil and iris may change due to contraction, dilation based on the illumination on eyes. Other factors like the distance from the imaging device, size of the eye/pupil, tilt of the head of subject being imaged should be considered. These factors contribute in capturing the same iris with differing characteristics. The location of the pupil does not need to be concentric under all the conditions [33]. In order to have robust comparison considering the conditions, the iris image has to be normalized making them scale-invariant and pupil-dilation-invariant.

We have based our works on Daugman's rubber sheet model which is explained in the upcoming section.

3.4.2.1 Daugman's Rubber Sheet Model

The segmented iris image is taken as the input and the detected iris points in the image are transformed into a normalized image with doubly dimensionless pseudopolar coordinate system [33]. Each cartesian point within the iris region is mapped to a pair of polar coordinates (r, θ) with r in the range [0,1] and θ in angular range of [0,2π].

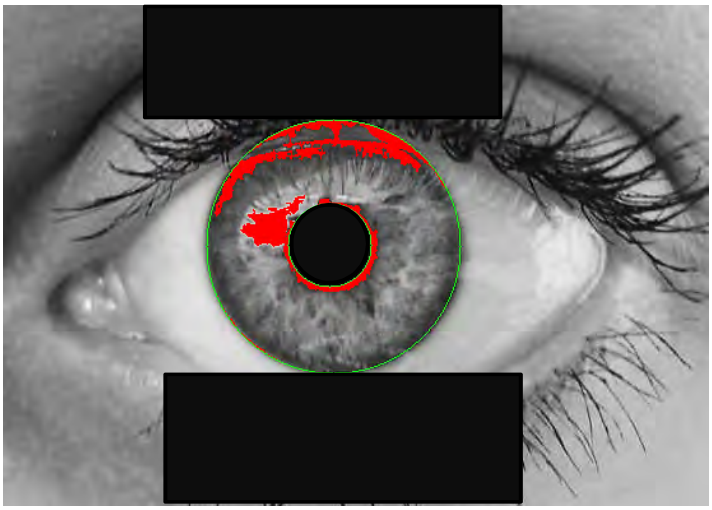

Figure 10: Iris image in cartesian co-ordinates given by $I(x(r,\theta), y(r,\theta))$

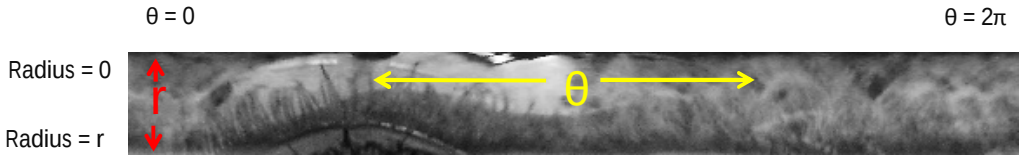

Figure 11: Normalized iris in polar co-ordinates

The whole process of normalization can be summed up as:

$$I(x,y) \rightarrow I(r,\theta) \tag{3.8}$$

where (x,y) represent the cartesian coordinates and (r,θ) represent the polar domain. Any co-ordinate pair, (x,y) in the transformed space $(x(r,\theta), y(r,\theta))$ is modeled as:

$$x(r,\theta) = (1-r)x_p(\theta) + r.x_i(\theta) \tag{3.9}$$

$$y(r,\theta) = (1-r)y_p(\theta) + r.y_i(\theta) \tag{3.10}$$

where x_i, y_i are the coordinates of iris boundaries and (x_p, y_p) are the coordinates of pupil boundaries along the θ direction.

Rotational inconsistencies are not considered in this case unlike the inconsistencies due to pupil dilation or distance from imaging device. The iris templates are shifted in the θ direction to align before the comparison [33].

3.4.2.2 OSIRIS : Normalisation

As the segmentated iris image does not necessarily correspond to circular shape, OSIRIS v4.1 uses non-parametric shape based normalisation [28]. The approach of Daugman's rubber sheet model uses a uniform sampling rate of θ_k, which meets the following two conditions:

$$\theta_k = 0 \qquad \text{for } k = 0 \tag{3.11}$$

$$\theta_k = 2\pi \qquad \text{for } k = W \tag{3.12}$$

Where θ_k is specifically provided by

$$\theta_k = \frac{k}{W} 2\pi \qquad k \in [0, W] \tag{3.13}$$

with W being the width and H being the height of the desired normalized image. In our work, we have used the width and height of 512 and 64 respectively.

However, OSIRIS v4.1 uses normalisation based on non-parametric shape and not on circle. Image of edges detected by employing the Viterbi algorithm is used as the input for the normalisation. The coarse contours on the image are selected such that there are least number of noisy gradients and thus sampling angle ϕ is not uniform.

With the new non-uniform sampling angle ϕ, the terms x_i, y_i and x_p, y_p corresponding to iris and pupil boundary mentioned in Equation 3.10 change to (x_i, y_i, ϕ_i) and (x_p, y_p, ϕ_p). The points (X_K^p, Y_K^p) corresponding to Equation 3.13 is approximated by interpolating two points j and $j+1$:

$$X_K^p = (1-\alpha) * x_p^j + \alpha * x_p^{j+1} \tag{3.14}$$

$$Y_K^p = (1-\alpha) * y_p^j + \alpha * y_p^{j+1} \tag{3.15}$$

where α is derived from the non-uniform sampling angle at both the points considered for the interpolation:

$$\alpha = \frac{\theta_k - \phi_p^j}{\phi_p^{j+1} - \phi_p^j} \tag{3.16}$$

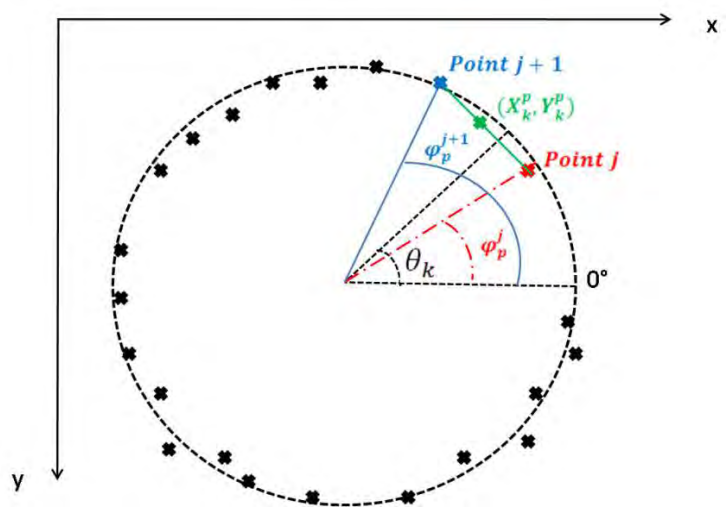

Figure 12: Computation of iris boundary point X_K^p, Y_K^p in OSIRIS
(Image credit : Sutra et al.[1])

[1]"http://svnext.it-sudparis.eu/svnview2-eph/ref_syst//Iris_Osiris_v4.1/doc/"

Figure 12 shows the relation between the sampling angle θ, non-uniform sampling angle ϕ and the located boundary co-ordinate. In the lines of Equation 3.14 and 3.15, the boundary for the pupil are also located. It has to be noted that the center of the iris and the pupil do not necessarily correspond to same point. The reader is further recommended to refer "Biometric Reference System" [28] for details on this method.

3.4.3 Iris Feature Extraction

The pattern of the iris is unique to each individual. To use it as a biometric feature, the discriminating information in an iris has to be extracted. The feature extraction schemes employed in this work are presented in this section.

3.4.3.1 2D Gabor Features

Gabor filters belonging to the class of bandpass filters are generally used for feature extraction and texture analysis among many other applications. The impulse response of a Gabor filter is formed by multiplying a complex sinusoidal carrier with a Gaussian envelope. The mathematical form of Gabor filter impulse, $g(x, y)$ is given by :

$$g(x, y) = w(x, y) * s(x, y) \tag{3.17}$$

where $s(x, y)$ constitutes complex carrier signal and $w(x, y)$ forms the Gaussian envelope, represented as :

$$w(x, y) = e^{\frac{-(x^2 + y^2)}{\sigma^2}} \tag{3.18}$$

The complex sinusoidal signal is represented mathematically as:

$$s(x, y) = e^{j(2\pi(u_o x + v_o y) + \psi)} \tag{3.19}$$

with u_o and v_o representing the frequency of the horizontal and vertical component of complex sinusoid. The term ψ represents the phase shift. The complex carrier signal can be separated into real and imaginary parts such that :

$$Re(s(x, y)) = Cos(2\pi(u_o x + v_o y) + \psi) \tag{3.20}$$

$$Im(s(x, y)) = Sin(2\pi(u_o x + v_o y) + \psi) \tag{3.21}$$

The real and imaginary components are the even symmetric and odd symmetric components. The Gabor filtered components of the symmetric and asymmetric components are:

$$g_{sym}(x, y) = e^{\frac{-(x^2 + y^2)}{\sigma^2}} * Cos(2\pi(u_o x + v_o y) + \psi) \tag{3.22}$$

$$g_{asym}(x, y) = e^{\frac{-(x^2 + y^2)}{\sigma^2}} * Sin(2\pi(u_o x + v_o y) + \psi) \tag{3.23}$$

The 2D Gabor filter over the image domain (x, y) is:

$$G(x, y) = e^{-\pi[(x - x_o/\alpha^2) + (y - y_o/\beta^2)]} e^{-2\pi i[u_o(x - x_o) + v_o(y - y_o)]} \tag{3.24}$$

where (x_o, y_o) specify position in the image, (α, β) specify the effective width and length, (u_o, v_o) specify modulation[33].

Based on the previous studies of Oppenheim and Lim [40], phase information is deemed to be highly significant compared to its counterpart of amplitude information.

Based on this, Daugman demodulates the phase information of output of Gabor filter and quantizes into four levels corresponding to all quadrants in the complex plane which are represented using two bits of data. A total of 2,048 bits and an equal number of masking bits are used in the template and its corresponding mask respectively. For the complete details on the 2D Gabor based iris features, the reader is advised to refer Daugman [33].

3.4.3.2 1D Log Gabor Features

Although, Gabor filters provide best simultaneous localization of spatial and frequency information, the maximum bandwidth is limited to one octave and are also not optimal for broad spectral information with maximal spatial localization. Field [41] proposed Log-Gabor filters with arbitrary bandwidth which could be optimised to produce a filter with minimal spatial extent. The impulse response of the Log-Gabor function is given as:

$$G(f) = exp\left(\frac{-[\log(f/f_o)]^2}{2.[\log(\sigma/f_o)]^2}\right) \tag{3.25}$$

where f_o is the central frequency of the bandpass filter, σ is the bandwidth.

To prevent the DC component whenever the bandwidth is larger than one octave, Masek et al. [34], used 1D Log-Gabor filter. Considering this a motivation, we have used 1D Log-Gabor as one of the techniques to extract the iris feature.

3.4.3.3 Modified Gabor Features

Ma et al. [42] proposed a scheme to capture the discriminating frequency information corresponding to local structure of the iris. Their approach was based on recommendations of Daugman [43] about the presence of high amount of information in frequency band of about three octaves.

In their method, a bank of filters is constructed to obtain the local texture information in spatial domain and two statistic values are used to represent each small region. All such information is used to construct a feature vector. To much of the similarity to Gabor filter, the modulating signal is the only differing component. Ma et al. [42] use circularly symmetric sinusoidal function along with oriented sinusoidal function in original Gabor filters. This design of filter also retrieves information in all the orientations and thereby provides high angular information corresponding to horizontal direction in normalized image.

3.4.3.4 Cell Based Cumulative Iris Code

Ko et al. [44] proposed a method based on change point analysis [45], which can be classified under cumulative-sum-based method for feature extraction. Their method consisted in dividing normalized iris image into cells of size $3\ rows \times 10\ columns$. Average grey value of the cell is used to represent the region for calculation. Each of the cell is grouped horizontally and vertically as shown in Figure 13. A group of 5 cells have reported better results according to their experiments.

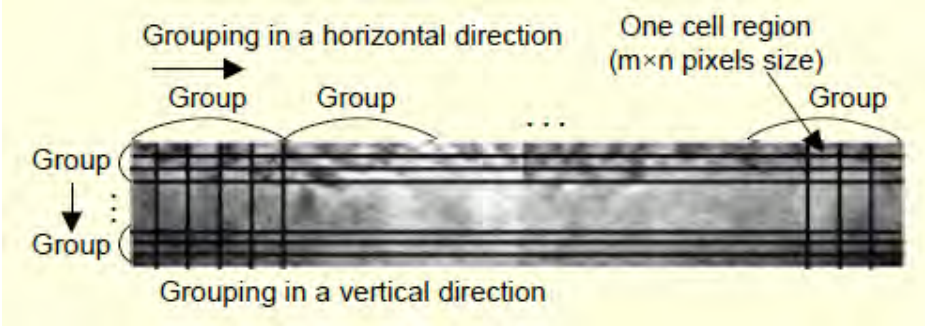

Figure 13: Ko et al.'s feature extraction scheme : division of normalized iris image into cell and grouping of cell (Image credit : Ko et al. [44])

Cumulative sums over each group is obtained by series of addition and subtraction:

$$S_i = S_{i-1} + (X_i - \bar{X}) \qquad \text{for i = 1, 2, ... 5} \tag{3.26}$$

where $\bar{X}$ is the mean value of 5 cells. Iris code is generated by analyzing cumulative sums. The values between maximum and minimum are assigned 1 if they compose upward slope and are assigned 2 if they compose downward slope. The other bits outside the maximum and minimum range in the iris code is assigned 0. This approach is generally speedy as the iris code depends only on series of additions and subtractions.

3.4.3.5 Local Intensity Variation Based Iris Features

Rathgeb and Uhl [46] proposed a feature extraction algorithm based on local intensity variation in iris. They extracted what is called as 'pixel-paths', by tracing intensity variations in horizontal stripes of distinct height [46].

1. Unwrapped iris texture of height h, length l is divided into n different horizontal texture stripes.
2. Two pixel-paths corresponding to light and dark intensity variations are created for each texture strip obtained from Step 1.
3. Starting from the leftmost center of the each strip, elements of light and dark intensity paths are computed by taking the maximum and minimum of three directly neighboring pixel values in previous and next column correspondingly.
4. Small peaks within a range are discarded by using a threshold and the final smoothed data is stored as the feature.

The size of the generated template is highly dependent on the height of unwrapped iris image.

3.4.3.6 Context Based Iris Feature

Rathgeb and Uhl [47] proposed an iris feature vector extraction scheme to use the most constant parts of iris-codes. Preprocessed iris textures are discretized to obtain a rather trivial iris-codes by detecting and removing most constant parts. The preprocessed iris images are divided into the blocks of $x \times y$ pixels to discretize by mapping the grayscale values of all included pixels to a natural number less than a predefined threshold k. The entire block is assigned the average value of all pixels which define the codeword of the

block. A two-dimensional iriscode is obtained by concatenating the resulting codewords of all discretized $x \times y$ pixel blocks.

3.4.4 Iris Feature Comparison

The feature extracted using the schemes mentioned in Section 3.4.3 are the representatives of the iris. They are compared against each other using the distance measures mentioned in the upcoming sections. For identifying an individual, one-to-many templates are compared and for verifying, one-to-one templates are compared. In both of these cases, the probe sample is compared against the template stored in the database. A positive identification is achieved when the obtained distance value satisfies certain threshold condition.

3.4.4.1 Hamming Distance

In the context of information theory, Hamming distance is the measure of differences corresponding to each position of two strings of equal length. Hamming distance measures the minimum number of substitutions/changes required for converting one string into another. Owing to the high entropy of iris, its template provides high statistical improbability for two different irises to agree on the patterns given rich amount of unique features.

Daugman [33] proposed the most used measure in iris recognition, Hamming distance. Simple boolean Exclusive-OR (XOR) operator is applied to probe iris code and reference iris code. The degree of disagreement with pair of bits are detected using XOR operator. The original proposed measure also uses iris mask for reference and probe to compensate the errors introduced by eyelashes, eyelids, specular reflections, or other noise. In this case, the iris mask is combined with the iris code using a logical AND operation and the result is used to measure the difference [33].

If the two iris code bit vectors are denoted as $codeA$ and $codeB$ with corresponding mask bit vectors denoted as $maskA$ and $maskB$, Hamming Distance HD is given as:

$$HD = \frac{\| (codeA \otimes codeB) \cap maskA \cap maskB \|}{\| maskA \cap maskB \|} \tag{3.27}$$

The resulting HD is a fractional measure of dissimilarity with 0 being a perfect match and higher value corresponding to non-match.

3.4.4.2 Hamming Distance in Cell Based Cumulative Iris Code

Ko et al. [44] use Hamming distance as the measure for similarity. The difference in their method surfaces due to non-usage of mask for iris. Normalized HD with respect to the length of the string is given as:

$$HD = \frac{1}{2N}\left[\left(\sum_{i=0}^{N} codeA_h(i) \otimes codeB_h(i)\right) + \left(\sum_{i=0}^{N} codeA_v(i) \otimes codeB_v(i)\right)\right] \tag{3.28}$$

when $codeA_h(i) \neq 0, codeB_h(i) \neq 0, codeA_v(i) \neq 0, codeB_v(i) \neq 0$ with h, v corresponding to horizontal and vertical direction and N is the number of cell regions with a specified number of rows and columns (3 pixels by 10 pixels in our experiments).

3.5 Importance Of Focus In Iris Imaging

In spite of accuracy provided by iris recognition, focus of the iris image has to be good enough to achieve good recognition performance. Typically, the acquisition of an iris image is repeated until a satisfactory focus quality is obtained. This process is obtrusive and leads to discomfort of the subjects. Bad focused images lower the identification rate impacting the genuine verification. One of the possible approaches is to avoid the problem of focus is to capture the iris video and select the best possible image. Some of the earlier works on addressing the problem of out-of-focus have proposed alternative methods [33, 48, 49, 50, 51]. In this work, we propose to use a Light-field Camera (LFC) to avoid the problem of focus during the capture process. LFC obtains multiple images at different focus or depth planes in single exposure. Therefore allowing the improvement in the focus of image after acquisition which helps in achieving better focused iris image and thereby aids in improving the accuracy of iris recognition. In this work, we propose a comparative study to evaluate the performance of iris recognition state-of-the-art methods using light-field and conventional cameras.

3.5.1 Image Quality In Iris Recognition

Image quality assessment has been an open issue in achieving good accuracy for iris recognition. Many researches are targeted towards assessing the optimum quality of the iris image for accurate recognition. Daugman [43] assessed the focus by measuring the power under 2D Fourier spectrum. Images passing certain threshold were used as the qualified images for recognition. Another work in assessing the quality was based on sharpness of the iris boundary to determine the focus quality [52]. Ma et al. [42] also devised methods to measure the focus quality of the image using the frequency distribution of the iris region. The coarse localization of pupil is used to extract two rectangular regions of fixed size adjacent to pupil. Fourier transform of these regions is analyzed and the decision on the focus quality is made with a Support Vector Machine (SVM) based decision system using the clusters formed by Fourier Transform. The most predominant low quality images come under:

1. Out-of-focus images (Defocused images)
2. Motion blurred images
3. Highly occluded images (Eyelids and eyelashes)

3.5.1.1 Out-of-focus Image

The increased or decreased distance of subject falling out of the focus range or depth-of-field of the imaging device results in out-of-focus images in general. Most of the available imaging devices have fixed focus distance at which the obtained image has highest quality. It has to be taken care to have the subject at the right distance to obtain the best focused iris image. Robust techniques to obtain the optimum quality image replicating the original scene are not present for iris imaging.

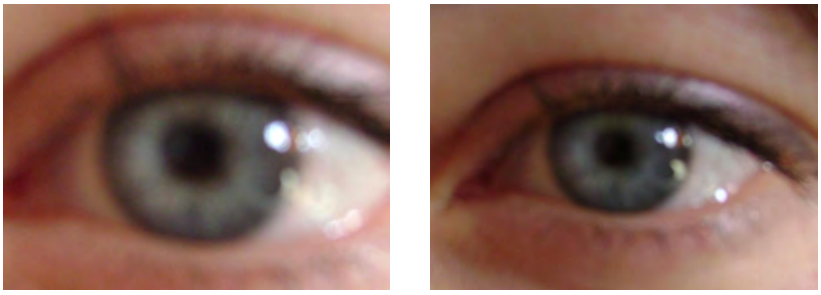

(a) (b)

Figure 14: Out-of-focus images in conventional iris imaging; (a) and (b) show the out-of-focus iris images with no clear visibility of iris pattern.

Figure 14(a) and Figure 14(b) illustrate the out-of-focus images. It can be noted from the images that the pattern of the iris from the image does not contain distinguishing texture information. Lower amount of texture information in the iris image impacts the performance of the iris recognition system.

3.5.1.2 Motion Blurred Images

Much like any other natural activities of human body, blinking is an automatic and periodic action. The rate of blinking increases in proportion to dryness in the human eyes to maintain adequate moisture in the eyeball. Irritation caused due to dust or infection also enhance the rate of blinking. At the time of acquisition of iris image, if the eyes being captured undergo motion due to a blink or if the subject moves, the captured iris is blurred resulting in a motion blurred iris image. Typically in the motion blurred iris image, edge boundaries are jagged in horizontal or vertical direction depending on the direction of motion. These kind of acquisitions result in inaccurate segmentation owing to absence of clear demarcation boundaries in the pupil and iris region. These images do not contain the features with high details as the texture information is also jagged.

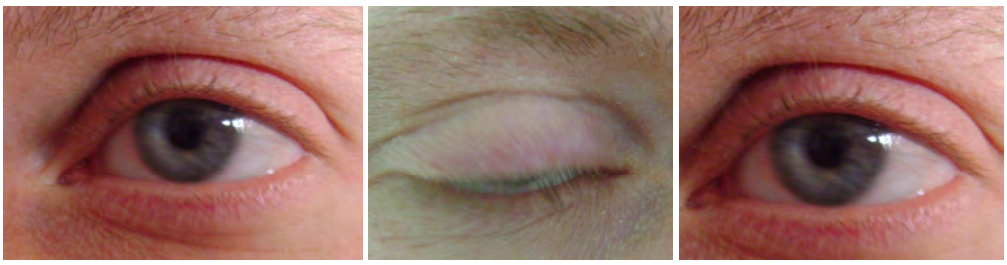

(a) (b) (c)

Figure 15: Motion blurred images

Figure 15 illustrates the motion blurred images. The images do not present the texture information in Figure 15(a) and Figure 15(c). Figure 15(b) shows the jagged pixels resulting due to a motion blur of the eye-lid.

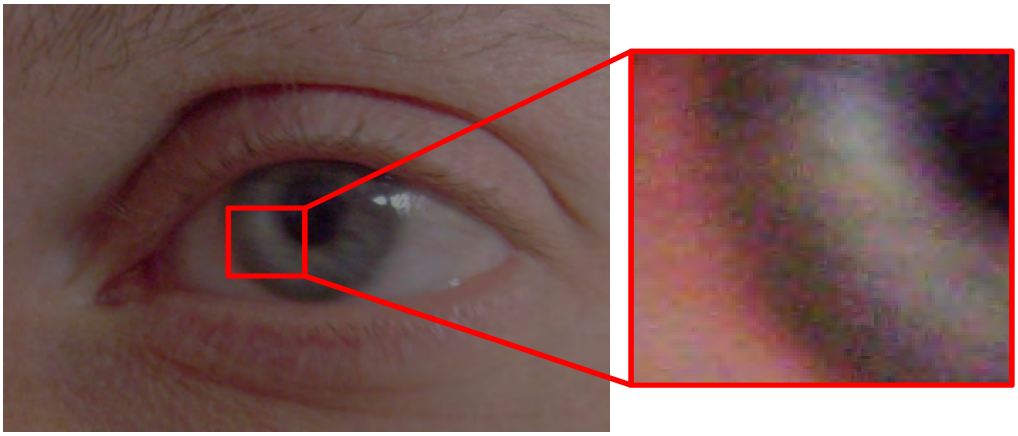

Figure 16: Motion blurred image and magnified iris region

Figure 16 shows the unclear image boundaries resulting from the motion blur. It can be seen from the image that the edges formed by eye-brows are still in focus whereas the eyeball is under motion. The movement of eyeball results in unsharp boundary between pupil and iris. The magnified region next to the image shows the blurred pixels and unclear region marking boundaries.

3.5.1.3 Occluded Iris Images

If the subject is not constrained to keep the eyes wide open in order to see the complete iris, iris image obtained is occluded image. The occluded iris image results in lesser number of features and thus increasing the Hamming Distance difference between the reference and probe sample. Although the threshold in the Hamming distance allows some amount of occlusions, if the iris image capture results in iris with more than 30% of occlusion, the recognition system is expected to have degenerative performance.

Figure 17: Prominently occluded iris images

Images shown in the Figure 17 exemplifies occluded image. The two things causing the occlusion is eye-lids and the eye-lashes. The eye lashes also cause the shadows if the illumination is not in the right direction. This problem of shadow is not seen in the Near Infra Red (NIR) acquisition but can be clearly seen in the visible spectrum. The image acquisition in this work has been carried out in visible spectrum which has resulted in the shadows of eye lashes in the iris region.

3.5.1.4 Other Artifacts

In the case of visible spectrum acquisition, there is a large likelihood of having the reflections in the image. The magnitude and the direction of reflection depends on the position of the imaging device and the position of the subject with respect to the illumination.

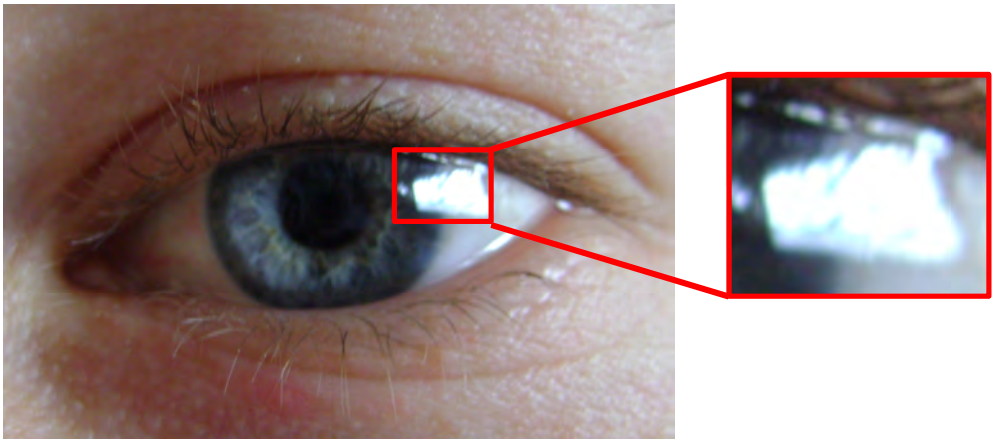

Figure 18: Reflections of illumination in iris image

Figure 18 shows the reflections on iris pattern due to the natural light. In this case, the region under the reflection cannot be used for iris pattern recognition and this information is used in creating the mask. The mask necessarily having the information of reflection is used for computing the Hamming distance between reference and probe iris.

Figure 19: Reflections due to eye-lash in iris image

Figure 19 shows another possible source for the loss of iris texture pattern. As shown in the image, the shadows of the eye lashes and the reflection of the imaging device pose a challenge in iris recognition. These kind of artifacts in the iris image are present in the visible spectrum acquisition under natural illumination. If these artifacts are not accounted during generation of the normalized iris and the corresponding mask, the performance of the iris recognition system decreases.

3.6 Discussion

This chapter has discussed the motivation for visible spectrum iris-recognition. A brief summary of state-of-the-art in the iris recognition framework has been presented. The techniques and framework employed in our work has been summarized. In particular, OSIRIS based segmentation and Daugman's rubber sheet model based normalization, followed by six different feature extraction schemes and Hamming distance based similarity measure have been discussed. Further, predominant image quality issues in iris recognition have been presented with various examples.

4 Light-field Iris Recognition

4.1 Motivation For Light-field Iris Imaging

Although a number of different challenges are mentioned in Chapter 3, we limit our work to address the out-of-focus issue in iris imaging. The use of conventional or existing 2D sensors in iris imaging have a constant focus constraining the subjects to be positioned at a fixed distance. This becomes important to obtain the best focus image with high texture information. With the risk of subject not being under fixed position, especially in at-a-distance scenario, the present day conventional iris imaging systems in visible spectrum are limited in providing best-focus iris images. The oblique shape of the eye also poses additional challenge in obtaining the best focus in all the regions of iris.

Various approaches to address the problem of focus have been devised. Narayanswamy et al. [48] & Boddeti and Kumar [49] have explored the wavefront coded imaging for iris recognition systems. The key idea in their approach is to improve the overall sharpness of the image using wavefront coding. Park and Kim [50]used the spectral-reflection from the IR-LED illuminator as a feedback information to set the focus and zoom. Daugman [33] measured the power in 2D Fourier spectrum to assess the image's focus quality. More recently, Tankasala et al. [51] have proposed a video based hyper-focal imaging. The video frames are captured under various focus for a specified duration. The captured frames under different focus are fused to obtain improved focus image for iris recognition. Extending the depth-of-field results in the decreased dynamic range and low SNR of the obtained images. Further, video based methods use sequence of frames which demand high amount of memory and computation along with the need for more acquisition time.

In this work, we propose a novel scheme to address the issue of out-of-focus by employing light-field or plenoptic imaging techniques. We have adopted first available consumer Light-field Camera(LFC) by Lytro Inc [14] for iris imaging. Summarizing the principle of LFC as described in Chapter 2, the plenoptic/light-field cameras are constructed by inserting a micro-lens array [6] or a pin-hole array or masks [11] between the sensor and main lens of camera. The presence of these micro lens (or array of pin-holes or masks) measures the total amount of light intensity deposited on the sensor and the direction of each ray from the incoming light. By re-sorting the measured rays of light with respect to their point of termination, a number of sharp images focused at different depths can be obtained. Light-field camera offers the following key advantages:

1. Generates images at different focus (or depth) in single exposure.
2. It is a low cost device.
3. Portable and hand-held.
4. Provides real-time exposure with no shutter lag.

With the number of advantages provided by the light-field camera, multiple depth or focus images obtained can be exploited to:

1. Obtain refocus images : Multiple focus images can be used to obtain an image with specific regions in the image at focus.
2. Obtain all-in-focus images : An all-in-focus image with all the regions in best focus can be obtained using all of the different depth images.
3. Estimate depth : Different focus images can be used to compute the depth of the scene through multiple focus/depth images.
4. Obtain synthetic aperture image : The different focus/depth images can be used to compute the synthetic aperture image.

In this work, we have exploited multiple depth images to obtain single all-in-focus iris image to address the issue of out-of-focus image. The proposed framework for addressing the issue is given in the upcoming sections.

4.2 Proposed Framework For Iris Recognition

Unlike in the regular iris acquisition scenario, where a normal 2D sensor or conventional camera is used, we have employed a light-field camera. More specifically, in this work we have employed the first available consumer light-field camera from Lytro Inc. [14].

4.2.1 Block Diagram

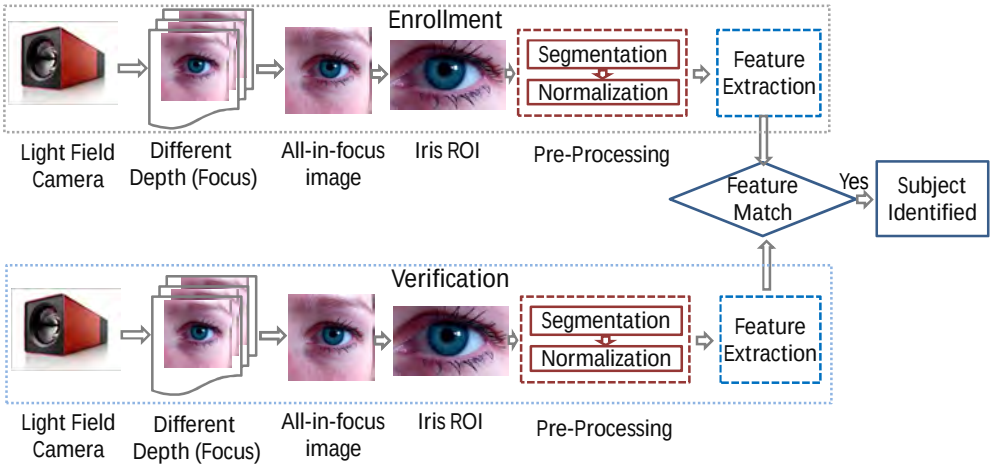

Figure 20: Proposed scheme for iris recognition

Figure 20 shows the proposed scheme for iris recognition. The proposed scheme consists of four major blocks: (1) Iris capture (2) ROI generation (3) Pre-processing (4) Verification.

4.3 Iris Capture

The first part of the proposed scheme consists of iris capture using the light-field camera. Iris images are captured in the visible spectrum with the light-field camera. The capture yields multiple depth/focus images from single exposure. An all-in-focus image

is obtained (Refer Section 4.3.2) from the different depth images. All-in-focus image is further used for the iris recognition after obtaining the region of interest (ROI) consisting of only eye region.

4.3.1 Light-field Iris Capture

Currently, two different light-field cameras are marketed by Raytrix GmBH [13] and Lytro Inc. [14]. Whereas the light-field cameras marketed by Raytrix GmBH are customer cameras customized for specific purposes, Lytro light-field cameras are consumer cameras and are priced at very low cost. As the Lytro light-field cameras are portable and easy to handle, we have employed Lytro LFC in our work.

Lytro light-field camera employed in this work has a sensor resolution of 11 Megarays with an effective spatial resolution of 1080×1080 pixels. The effective spatial resolution is reduced due to re-sampling of the 4 dimensional light-field data. No additional optics were added to the camera in our work.

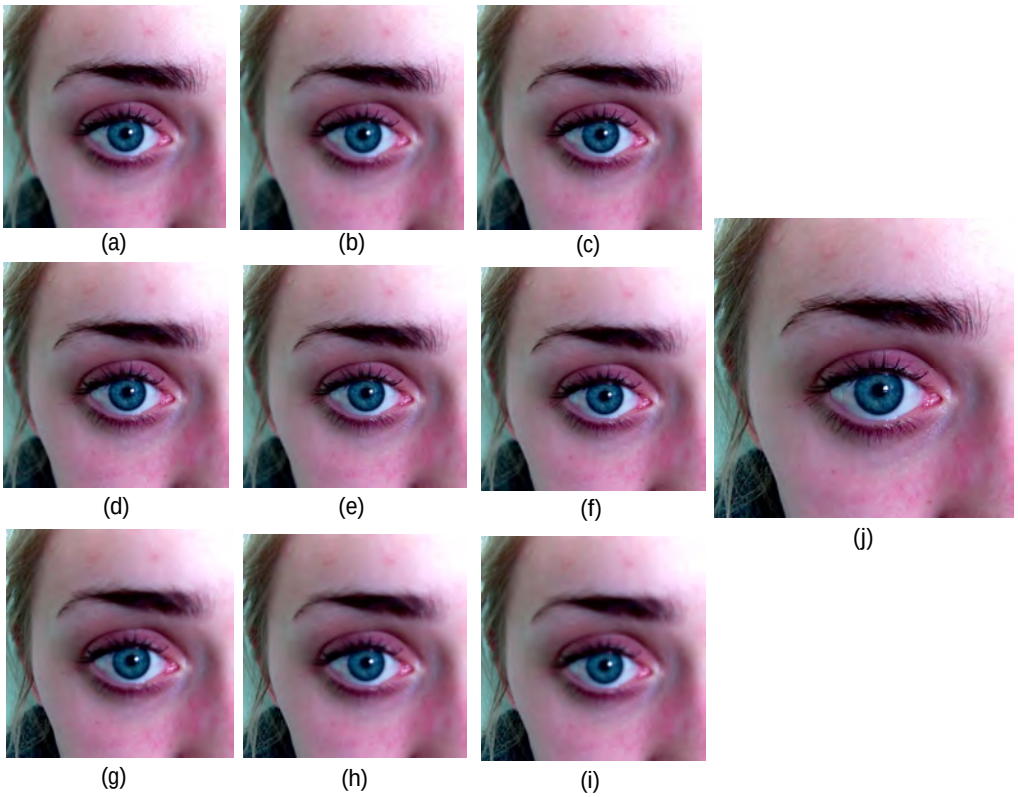

Figure 21: Different focus images obtained from single exposure. (a) - (i) correspond to multiple focal planes and (j) is the obtained all-in-focus image

Thus, with the motivation of obtaining multiple images, we have employed the light-field camera for iris capture that results in number of images according to the focal length being captured. Figure 21 shows multiple images obtained for single subject. Figure 21(a) - Figure 21(i) show the images with sharp regions in different parts. Figure 21(j) shows the corresponding all-in-focus image obtained. Figure 22 exemplifies the variation of sharpness in different depth images. It can be observed that Figure 22(a 3) is in focus

while Figure 22(a 1) and Figure 22(a 2) show the non-sharp regions in Figure 22(a). In Figure 22(b), Figure 22(b 2) is in focus while the other two are not. In Figure 22(c), Figure 22(c 1) is in focus and Figure 22(c 2), Figure 22(c 3) are out-of-focus.

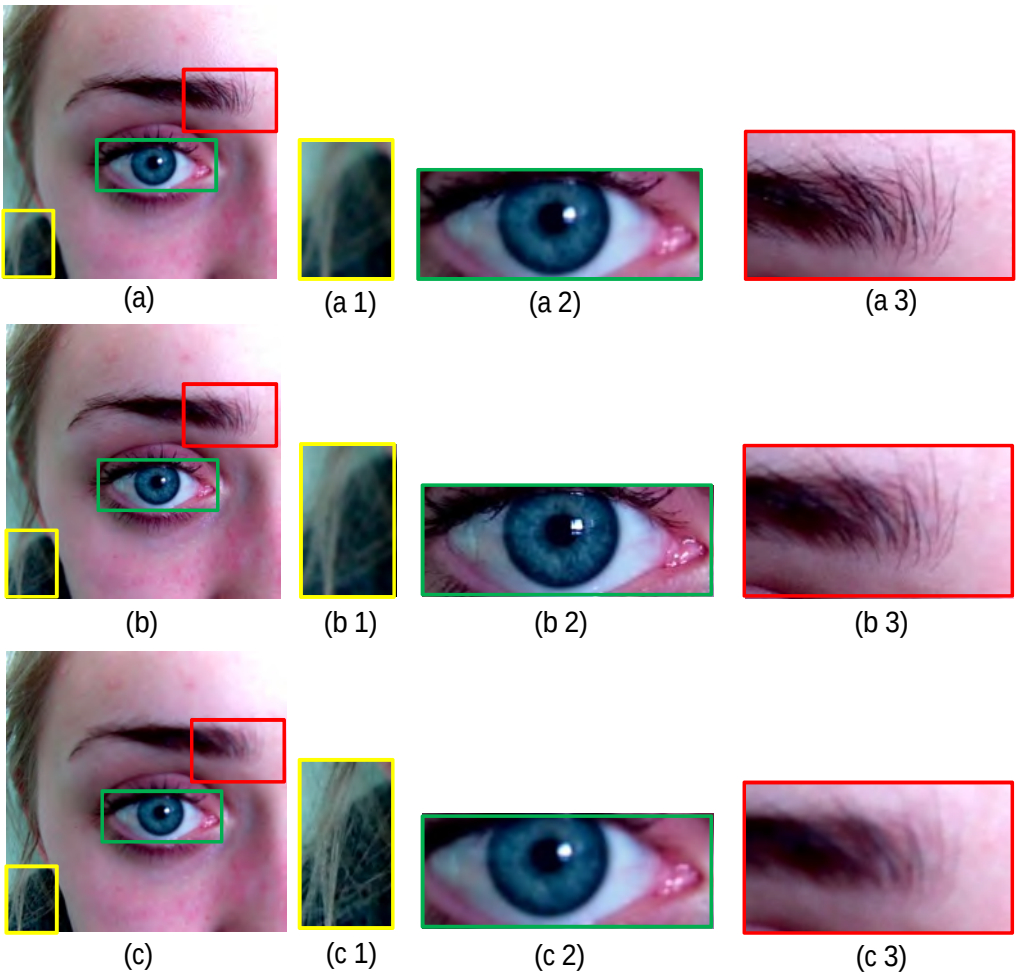

Figure 22: Varying sharpness in different regions of image

Thus our interest lies in exploiting multiple focus images to obtain an all-in-focus image for robust iris recognition.

4.3.2 Generating All-in-focus Image

Each sample acquired by the light-field camera in this work results in a raw file consisting of a set of images along with the meta information of the regions of focus. These images are not uniformly focused and they have sharpness in different regions. This information is used to retrieve the all-in-focus image. (Refer Figure 21 (j) for sample all-in-focus image). The obtained information on the sensor is used to construct multiple depth images. Each image corresponds to different focus, depth and angle of imaging.

In this work, we have employed the *"LFP (Light Field Photography) File Reader Ver-*

sion 2.0" [1] developed by Behnam Esfahbod under the terms of the GNU General Public License to generate multiple-refocus images and all-in-focus image.

4.3.2.1 All-in-focus Iris Image

As mentioned in previous sections, the problem of out-of-focus iris image is predominant in conventional camera. The light-field camera offers a better edge in terms of focusing after the acquisition. This enables to obtain better quality iris image with good focus. Figure 23 illustrates the winning factor of all-in-focus for light-field camera. Figure 23 (a) and Figure 23 (b) show the out-of-focus iris image obtained for a single subject. Figure 23 (c) and Figure 23 (d) show the better quality iris image obtained for the same subject in light-field camera. The focus and the sharpness of all-in-focus iris image in the latter part is superior. This is the key motivation for our proposed scheme.

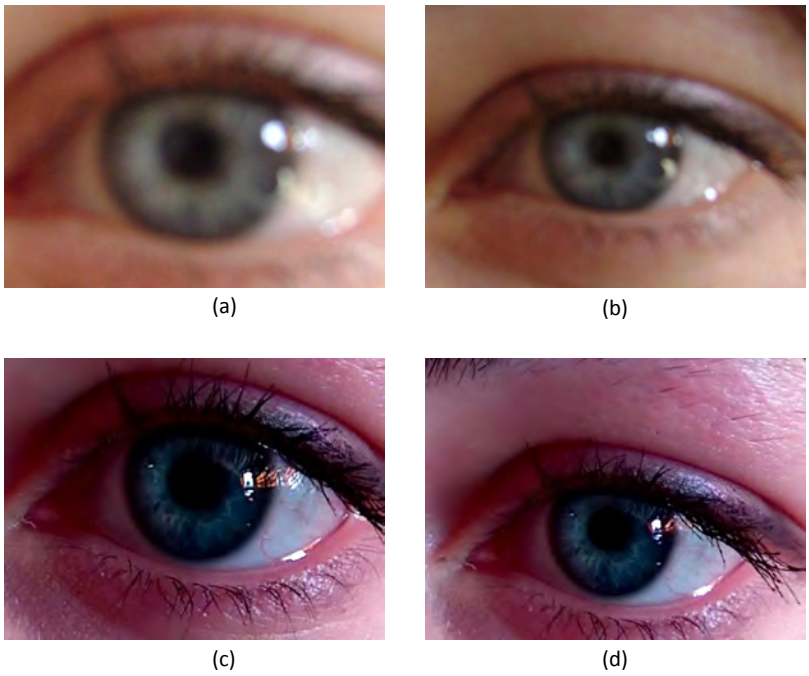

Figure 23: Illustration of out-of-focus image; (a) and (b) show the out-of-focus iris image captured using the conventional camera; (c) and (d) portray the all-in-focus iris image captured using light-field camera.

The iris pattern visibility and texture information obtained from the all-in-focus image is highly detailed. Higher details of the texture structure proportionately increases the recognition/verification accuracy. Figure 24 (a)-(d) show the iris pattern visible in different focus images. Figure 24 (e) shows the iris pattern at the best available detail.

[1] The source code to extract all-in-focus image is available at `"https://github.com/behnam/python-lfp-reader"`

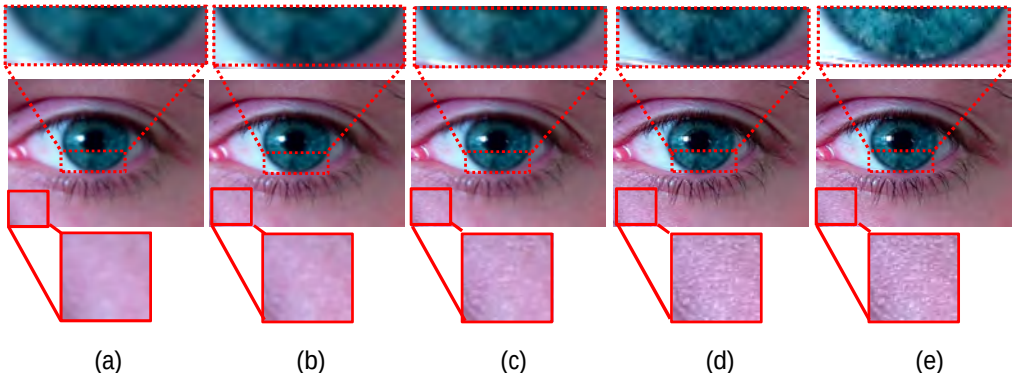

Figure 24: Sharpness and details in depth images; (e) shows highest amount of information in terms of sharpness.

4.4 Data Preprocessing

The images captured from conventional and light-field camera do not just have the eye region. The images also have the periocular region, parts of background and other parts of head like hair in the field of view. In order to obtain best segmentation results, it becomes necessary to extract the region consisting of eye. Figure 25 exemplifies the necessity for pre-processing images in order to obtain accurate segmentation. Most of the segmentation schemes need an approximate radius of circle to estimate the iris and pupil region and thus the chances of detecting the false iris region increases with the presence of lighter region around a darker spot. In the case of Figure 25(a), the original image has been captured along with the background. This results in the detection of boundary between background and hair region as shown in Figure 25(b). The segmentation on the extracted ROI consisting of the eye region from the original image shows robust segmentation. It has to be noted that the extracted ROI does not necessarily provide the best segmentation owing to many other parameters. However, the study of robustness of the segmentation schemes is beyond the scope of this work.

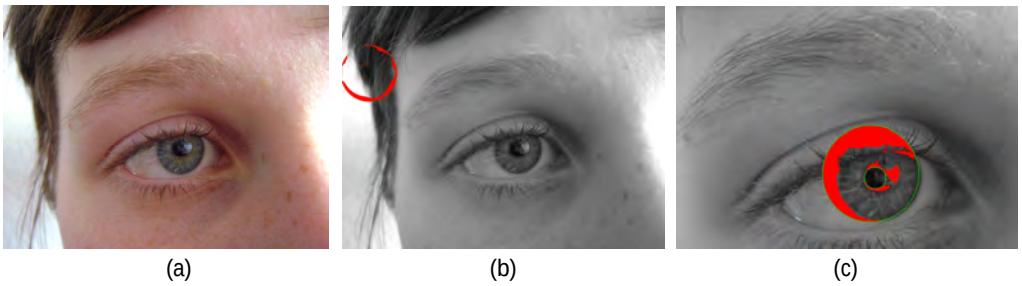

Figure 25: ROI detection for accurate segmentation; (a) Original captured image (b) Wrong segmentation (c) Right segmentation on cropped ROI

Deriving the motivation from the aforementioned argument, the images captured using both conventional camera and light-field camera are pre-processed to extract the eye region which is of interest for our work. The idea behind obtaining the region of interest is to exploit the presence of the pupil in the image which corresponds to darkest region surrounded by white sclera/eyeball.

The general outline of the algorithm is mentioned in the steps below:

1. Transform the image from RGB to YC_bC_r (Luma - Chroma Blue - Chroma Red) color space. For a given pixel (x, y), YC_bC_r representation of an RGB image $I_{rgb}(x, y)$ with $(x\ rows \times y\ columns)$ is :

$$I^T_{YC_bC_r}(x, y) = \begin{pmatrix} 0.299 & 0.587 & 0.114 \\ -0.1687 & -0.3313 & 0.5 \\ 0.5 & -0.4187 & -0.0813 \end{pmatrix} I^T_{rgb}(x, y) + \begin{pmatrix} 0 \\ 128 \\ 128 \end{pmatrix}$$

$$I_Y(x, y) = I_{YC_bC_r}(x, y, 1)$$
$$I_{C_b}(x, y) = I_{YC_bC_r}(x, y, 2)$$
$$I_{C_r}(x, y) = I_{YC_bC_r}(x, y, 3)$$

2. Subtract Chroma-red channel from Chroma-blue channel as given in by:

$$I_{diff}(x, y) = I_{C_b}(x, y) - I_{C_r}(x, y);$$

3. Convert the obtained difference image $I_{diff}(x, y)$ to binary image using Otsu's local threshold method to localize the sclera region. The brightest part in the image corresponds to the sclera.
4. Obtain the bounding box of largest area in the thresholded image. Discard the regions touching the image boundaries.
5. Determine the centroid of the largest bounding box. This region corresponds to the approximate eye region.
6. Enlarge the bounding box in the direction of x and y using the distance between detected bounding box and the centroid. Enlarged bounding box makes sure of obtaining complete eye region including some periocular region.
7. Crop the original RGB image I_{rgb} using the co-ordinates of the computed (extended) bounding box.

Figure 26 (a) shows the captured original image in RGB color space. Figure 26 (b), 26 (c) and 26 (d) show the corresponding image in Luma channel, Chroma-blue channel and Chroma-red channel.

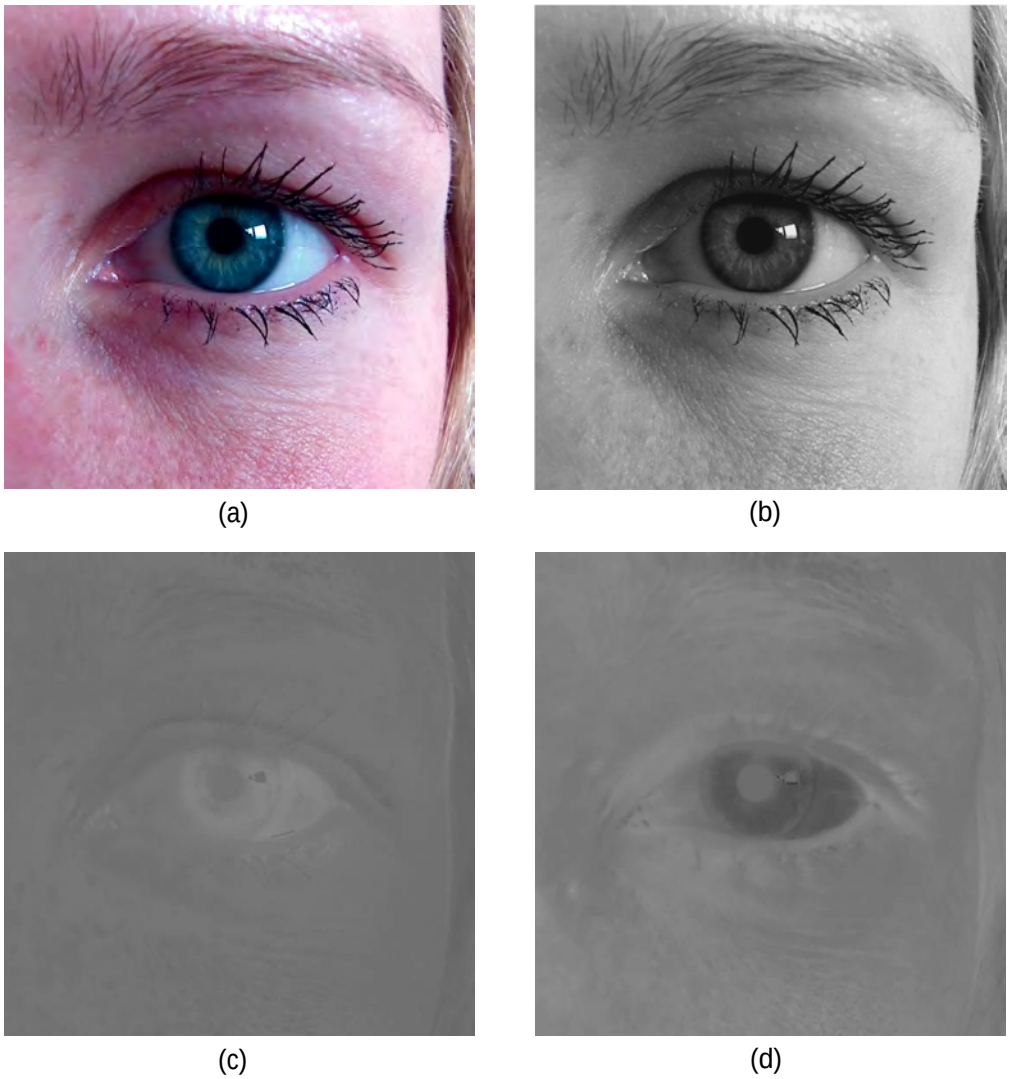

Figure 26: Image in RGB colorspace and YC_bC_r colorspace; (a) Original RGB Color space, (b) Y channel (c) C_b Channel and (d) C_r Channel

The difference between the C_b and C_r channel is shown in the Figure 27 (a). Taking the clues from sclera presenting some information due to its whiteness, we threshold the difference image to localize the exact eye region using Otsu's method as depicted in Figure 27(b). Figure 27(c) shows the largest area detected in the image. It can be noted from the image that parts of the iris region are not completely obtained. To obtain the complete iris pattern, we extend the bounding box as mentioned previously. Figure 27(d) shows the extended bounding box computed using the ratio between the centroid and the edges along the horizontal and vertical direction. Figure 28 shows the obtained ROI with complete eye region. This image is then rescaled to a size of 640x480 pixels.

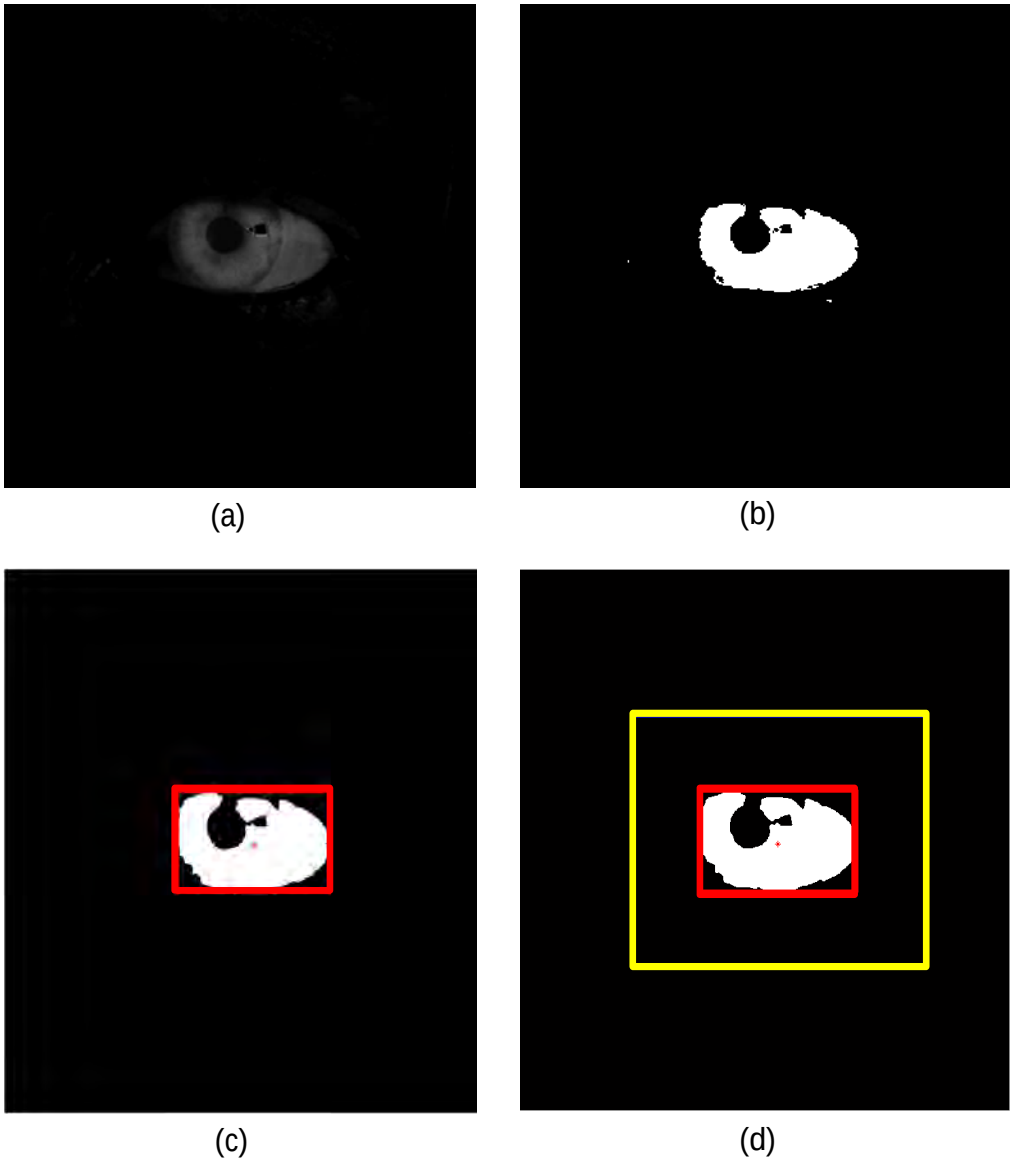

Figure 27: Bounding box for ROI generation to extract eye region. (a) Difference in C_b and C_r (b) Binarized difference image (c) Bounding box for largest area (d) Extended bounding box to cover complete eye region

Figure 28: Cropped ROI image with eye region

4.5 Preprocessing And Recognition

The extracted ROI image is processed through the normal pipeline of iris recognition which includes segmentation, normalization and feature extraction followed by verification. The segmentation includes isolation of eye-lids, eye-lashes and iris pattern by marking the clear boundaries between the eye-lids, eye-lashes and iris-pupil boundary. The segmented image is then normalized to a rectangular image. Iris features are extracted from the normalized image and the corresponding features of the reference iris and probe iris are matched using the Hamming distance measure for verification. In this work, we primarily focus on the application of light-field camera for iris recognition and hence, we have employed the existing standard algorithms and techniques for evaluating the proposed framework. We have based the segmentation scheme on the OSIRIS framework mentioned in the Section 3.4.1.4. We have evaluated the six different feature extraction schemes:

1. 2D Gabor Features [33]
2. 1D Log Gabor Features [34]
3. Modified Gabor Features [42]
4. Cell Based Cumulative Iris Code [44]
5. Local Intensity Variation Based Iris Features [46]
6. Context Based Iris Features [47]

Hamming distance measure is employed for iris matching between the reference and probe image.

4.6 Summary

In this chapter, the motivation for using light-field camera in the context of iris recognition has been discussed. A novel scheme for solving the problem of out-of-focus imaging in conventional iris recognition system has been introduced and the claim for the proposal has been supported by visual illustrations. The key advantages of using light-field camera for enhanced iris pattern visibility has been shown through various examples. The merits of proposed scheme has been discussed for the improvement of state-of-the-art in iris acquisition systems.

5 Light-field Iris Database

5.1 Existing Database For Iris Recognition

Iris recognition has been tried and tested on the Near Infra-Red (NIR) spectrum to obtain the complete texture information present in both lighter and darker iris. The main reason for using NIR is to capture the information present in the iris with higher melanin pigmentation which is known to absorb the light of shorter wavelength. Owing to this reason, many of the studies related to iris recognition have considered NIR acquisition and hence there is a considerable amount of open iris databases such as CASIA [53], UBIRIS [54] and ICE[55]. These datasets also contain a high number of samples which have been used for various studies on iris recognition. It has to be noted that, when acquiring the NIR iris image, controlled illumination in the NIR range has to be set up.

The number of publicly available iris database acquired in visible spectrum is rather low. Some of the visible spectrum open iris databases are UBIRIS v1, UBIRIS v2 [54] and UPOL [56]. Added to the availability of the lesser iris database acquired in the visible spectrum, there exists no iris database captured using the emergent and promising light-field imaging technology. Table 1 provides the list of major and publicly available iris databases. It can be seen that the majority of them are focused on NIR spectrum.

Table 1: Summary of major open iris databases.

Database	**Wavelength**	**Device**	**Images**
BATH	Near Infrared	ISG LightWise LW 1.3-S-1394	16000
CASIA v1	Near Infrared	CASIA Camera	756
CASIA v2	Near Infrared	CASIA Camera	2255
CASIA v3	Near Infrared	CASIA Camera	22051
ICE 2005	Near Infrared	OKI irispass-h	2900
ICE 2006	Near Infrared	LG EOU 2200	75000
MMU 1	Near Infrared	LG EOU 2200	450
MMU 2	Near Infrared	LG EOU 2200	995
UBIRIS v1	Visible	Nikon E5700	1877
UPOL	Visible	SONY DXC-950P 3CCD with TOPCON TRC501A	384
WVU	Near Infrared	OKI irispass-h	3099
Ubiris v2	Visible	Canon EOS 5D	11102

5.2 GUC Iris Database

In the context of non-availability of any light-field iris database, we have constructed a light-field iris image database. In order to have a baseline comparison with the conventional iris imaging systems, we have constructed a iris database acquired from the conventional 2D camera. Table 2 gives the number of images in our newly constructed database. The complete set of images for both conventional camera and light-field camera shall be made available to the public in future. This work contributes to the iris research community by providing the newly acquired iris database. The key outcomes of this part of the work are:

1. Providing the research community with two new iris databases acquired in visible spectrum
2. Providing the research community with the first available light-field iris database with 84 unique subjects with 5 samples each (total of 420 iris images).
3. Providing iris images focused at different depth (3387 refocus /depth images). This can be used to evaluate the state-of-the-art algorithms to validate the iris recognition accuracy with varying focus.
4. Providing a challenging iris dataset to facilitate the development and evaluation of new algorithms to enhance the iris recognition accuracy under low/distorted focus constraint (conventional and light-field).
5. Providing a non-ideal iris database corresponding to real-life scenario for visible spectrum acquisition.

Table 2: Summary of GUC iris databases.

Database	Wavelength	Device	Images
GUCCID	Visible	Sony DSC S750	420
GUCLID	Visible	Lytro	420 (All-in-focus) 3387 (Depth/focus images)

5.3 Experimental Set-up

Lytro light-field camera and Sony DSC S750 conventional camera was employed in this work. There was no additional optical lens used for both the cameras. The conventional camera was operated by mounting it on tripod at the distance of 9-12 inches from the subject. The camera was focused on the iris in the auto-focus mode with automatic ISO. Lytro light-field camera was also placed at a distance of 9-12 inches from the subject. Unlike the convetional camera, Lytro light-field camera supports only constant aperture of f/2.0 with automatic ISO. Table 3 gives the complete details of the parameters of conventional and light-field camera.

Table 3: Camera parameters for conventional and light-field camera employed.

Parameters	Conventional camera	Lytro light-field camera
Resolution	7 Megapixels	11 Megarays
Working Spatial Resolution	2304 x 3072	1080 x 1080
Sensor Type	CCD	CMOS
Sensor Size	25.4 x 63.5 mm	6.5 x 4.5 mm
Focal Length	5.8 mm - 17.4 mm	6.45 mm - 51.4 mm
Aperture Range	f/2.8 - f/9.7	Constant f/2.0
ISO	Automatic	Automatic

5.4 Description of GUCCID & GUCLID

The two iris databases constructed as a part of this work are:

1. Gjøvik University College Conventional Iris Database (GUCCID)
2. Gjøvik University College Light-field Iris Database (GUCLID)

Details of the databases are presented in the upcoming sections. This dataset is acquired under simulated real-life scenarios of contactless iris acquisition.

5.4.1 Less Constrained Iris Capture

Naturally protected by eye lashes and eye lids, human iris enables the contactless or at-a-distance iris capture. Many of the present day systems used for the face recognition can thus be modified to also capture the iris. Under the natural acquisition scenario, human eye is prone for movements. Added to it is the dilation of the pupil and whose size varies based on the intensity of the incoming light. Under the illumination of high amount of light, any person tends to close the eyes to a certain degree. This also results in the occluded iris pattern for acquisition. In order to simulate the real life scenarios, we have captured the iris in a less constrained environment motivated by the arguments put forward by Proenca et al. [54].

5.4.2 Gjøvik University College Conventional Iris Database (GUCCID)

GUCCID iris database was acquired using a conventional 2D sensor based camera, SONY DSC S750 with an effective resolution of 7.2 Megapixels and no additional optics. The conventional camera was mounted on a tripod at a fixed distance of around 15 inches from the subject's position. 5 samples were acquired for each subject with an interval of approximately 30 seconds between the sample acquisition. This dataset has resulted in total of 84 unique iris with 5 samples for each class (420 iris image samples, 84 unique iris).

5.4.3 Gjøvik University College Light-field Iris Database (GUCLID)

GUCLID iris database was acquired using the first available consumer light-field camera(LFC) from Lytro Inc [14]. The light-field camera employed in this work has an effective resolution of 1.2 Megapixels. The camera was held at a distance of approximately $10 - 15$ inches from the subject's face. Each sample was acquired in an interval of less than 30 seconds.

As the light-field camera provides multiple depth images, a total number of 3387 images have been obtained for 84 unique irises. Each sample acquired has varying number of depth images. The dataset has resulted in 420 all-in-focus images in total and thus 84 unique all-in-focus irises.

Figure 29(a) and 29(c) show the sample images from GUCCID database and Figure 29(b) and (d) show the all-in-focus images for the corresponding subject in GUCLID database.

Figure 29: Sample images from GUCCID and GUCLID Images. (a) and (c) show the images obtained from conventional camera available in GUCCID database; (b) and (d) show the images obtained from light-field camera for the corresponding subject in GUCLID database

5.5 Statistical Information of Database

GUCCID and GUCLID consists of iris images obtained from 22 male and 20 female subjects. The database consists of 70 unique light-colored iris which is constituted by light-blue and light-green iris. In addition to this, it also consists 10 unique amber colored iris and 4 dark iris. The dataset consists of people in the age group of 20-30 years. The complete distribution can be seen in the Figure 30, Figure 31 and Figure 32.

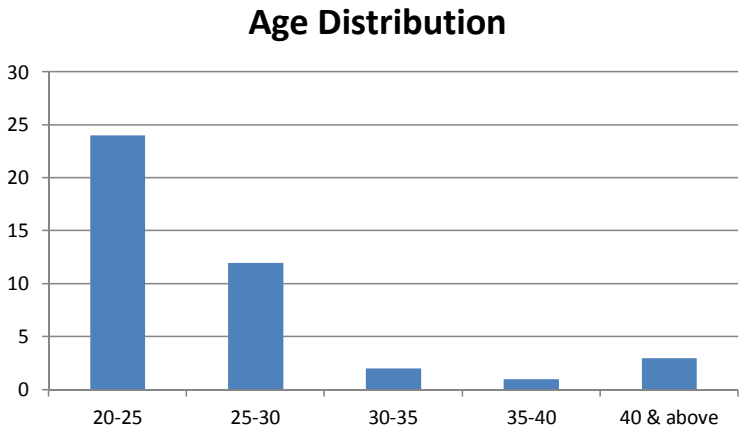

Figure 30: Age distribution in GUCCID and GUCLID database

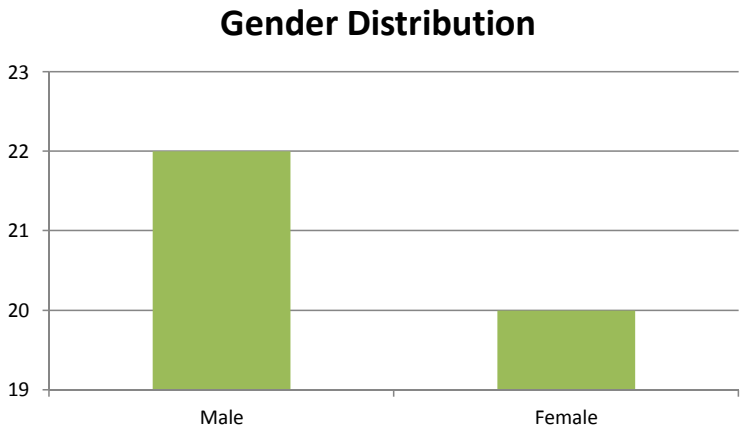

Figure 31: Gender distribution in GUCCID and GUCLID database

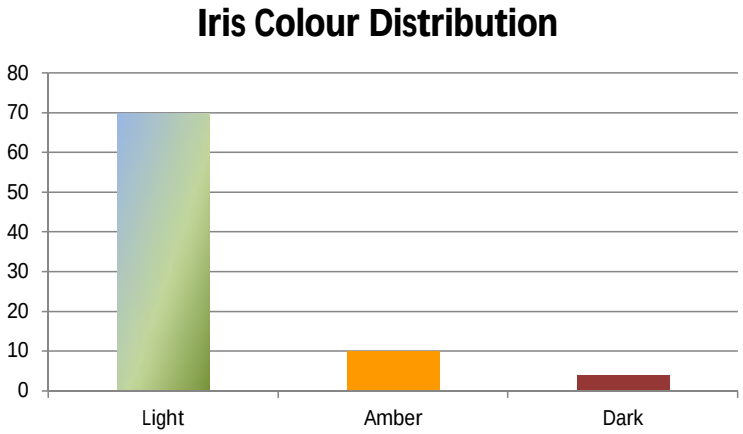

Figure 32: Iris color distribution in GUCCID and GUCLID database

5.6 Discussion

In this chapter, we have discussed the protocols used to create two new iris database captured from conventional and light-field camera. This chapter also highlights the importance of the newly acquired database for light-field iris recognition. To the best of our knowledge, this is the first available iris database captured using the light-field camera. Furthermore, these iris image databases shall be made available to the research community in near future.

6 Experimental Results

6.1 Data Acquisition

A total of 84 unique iris data obtained each from light-field camera and conventional 2D sensor based camera were used in this work. The experiments were conducted using 420 iris images corresponding to conventional camera and 420 all-in-focus images corresponding to light-field camera. 3387 depth images were used to obtain all-in-focus images from the light-field camera. The whole set of iris images was evaluated for the identification accuracy using the state-of-the-art schemes.

Statistical Computation

The results are presented in terms of Equal Error Rate (EER) which is defined as the point where the False Match Rate (FMR) equals False Non-Match Rate (FNMR) [16]. Receiver operating characteristic (ROC) graphs are shown for each of the algorithms and the value of 1-FNMR at lower FMR rates. Verification rates such as Genuine Match Rate, FNMR and FMR are computed as below:

$$GMR(t) = \frac{\|\Phi_g(t)\|}{\|\Phi_g\|}$$
$$FMR(t) = \frac{\|\Phi_i(t)\|}{\|\Phi_i\|}$$
$$FNMR(t) = 1 - GMR(t)$$

$where\ \Phi_g$is the set of all genuine similarity score
Φ_i is the set of all imposter similarity score
$\Phi_g(t)$ is the set of all genuine scores $s > t$
$\Phi_i(t)$ is the set of all imposter scores $s > t$

6.2 Conventional Camera

Preprocessed conventional images are segmented using the OSIRIS framework (Refer section 3.4.1.4). The choice of the OSIRIS method was based on the previous experimental works by Sutra et al. [39]. The segmented images are normalized using Daugman's method of rubber sheet model [33]. Corresponding masks for the normalized iris images are generated as well.

Unique features from the normalized images are then extracted for iris verification. In this work, we have evaluated the newly collected database GUCCID using 6 different feature extraction schemes listed below:

1. Daugman's 2D Gabor Features [33]
2. 1D Log-Gabor Features [34]
3. Context Based Iris Features [47]

4. Modified Gabor Features [42]
5. Local Intensity Variation Features [46]
6. Cell Based Cumulative Iris Features [44]

The distance between any two iris codes are measured using the Hamming distance with various thresholds for finding the genuine and imposter scores. Table 4 shows the scores obtained for various feature extraction schemes.

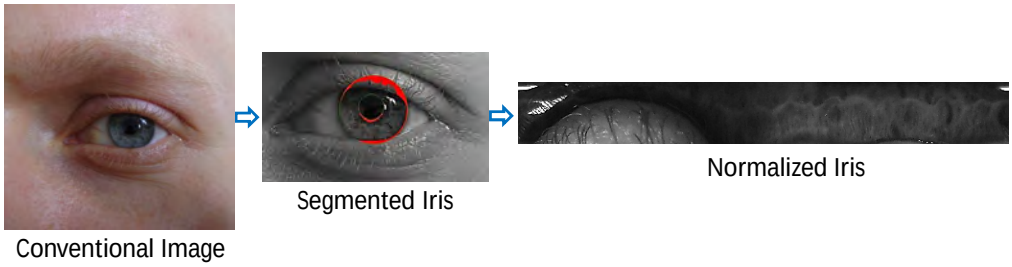

Figure 33: Normalization of iris for conventional camera image

6.2.1 Discussion

The results mentioned in the Table 4 demonstrate best results with an Equal Error Rate (EER) of 8.53% for 2D Gabor features proposed by Daugman [33] and the worst performance (highest rate of EER) is seen for the context based iris features with 27.38% EER.

6.3 Light-field Camera

The light-field camera provides multiple depth images focused at various regions. To obtain the best quality iris image, an all-in-focus image is generated. The all-in-focus image has all the regions in the image at the best possible focus for a given exposure. The obtained all-in-focus image is segmented using OSIRIS framework (Refer Section 3.4.1.4) owing to its better segmentation accuracy as cited by Sutra et al. [39]. Daugman's rubber sheet model [33] is employed for normalizing segmented iris images.

Unique features from the normalized images are then extracted for iris recognition. The schemes employed for feature extraction for images from conventional camera is employed for the images from light-field camera. This establishes a standard to compare the performance on an uniform scale (Refer Section 6.2 for the list of all schemes employed).

The distance between any two iris codes are measured using the Hamming distance with various thresholds for finding the genuine and imposter scores. Table 4 shows the scores obtained for various feature extraction schemes.

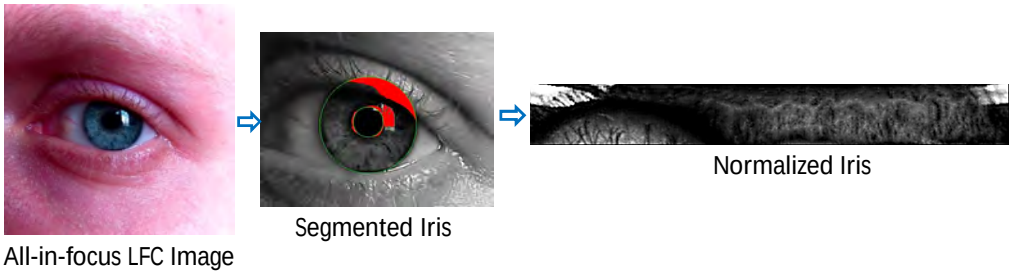

Figure 34: Normalization of iris for light-field camera image

6.3.1 Discussion

All-in-focus images obtained from the light-field camera reported an EER of 3.61% with 2D Gabor features proposed by Daugman [33] (Refer Table 4), while the highest rate of EER (worst accuracy) has been demonstrated for the context based iris features [47] with 22.21% EER.

6.4 Results

A total number of 84 unique iris with 5 samples were evaluated using six different schemes. This resulted in 840 genuine comparisons and 87150 imposter comparisons for each scheme. The individual scores obtained for both conventional camera and light-field camera are compared in the given Table 4. It can be observed that the light-field camera has performance score with lower EER showing promising recognition accuracy as compared to conventional camera. The best achieved EER of 3.61% is observed with light-field images using Daugman's 2D Gabor features. Some of the key considerations to be made in this observation is that the images acquired are closer to real life verification scenarios. This setup of data acquisition also has images with lower focus for conventional camera. The clear advantage of light-field camera is in obtaining the all-in-focus image which increases the recognition/verification accuracy. It can be noted that all of the feature extraction schemes have resulted in lower EER for light-field camera than counterpart conventional camera.

Table 4: Quantitative results obtained from various schemes for all-in-focus iris images.

Feature Extraction	EER (%)	
	Light-field Camera	Conventional camera
Rathgeb & Uhl [47]	22.21	27.38
Rathgeb & Uhl [46]	12.39	18.24
Ko et al. [44]	6.51	12.55
Ma et al. [42]	6.27	12.07
Masek et al. [34]	4.92	12.44
Daugman [33]	3.61	8.53

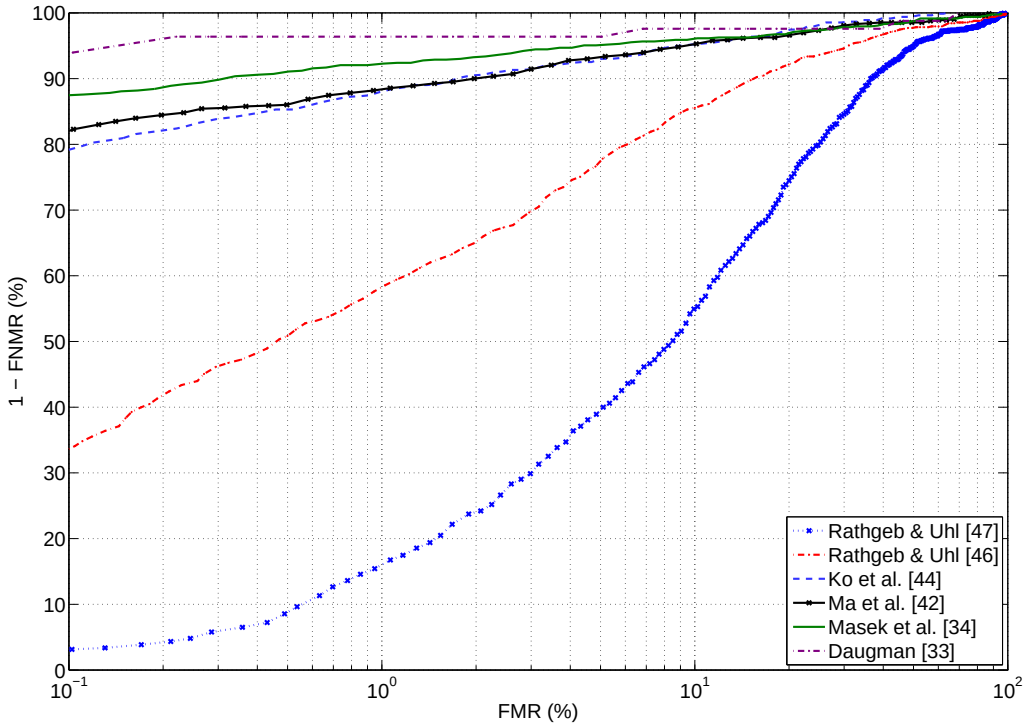

Figure 35: ROC Characteristics graph for all-in-focus iris images from Light-field Camera.

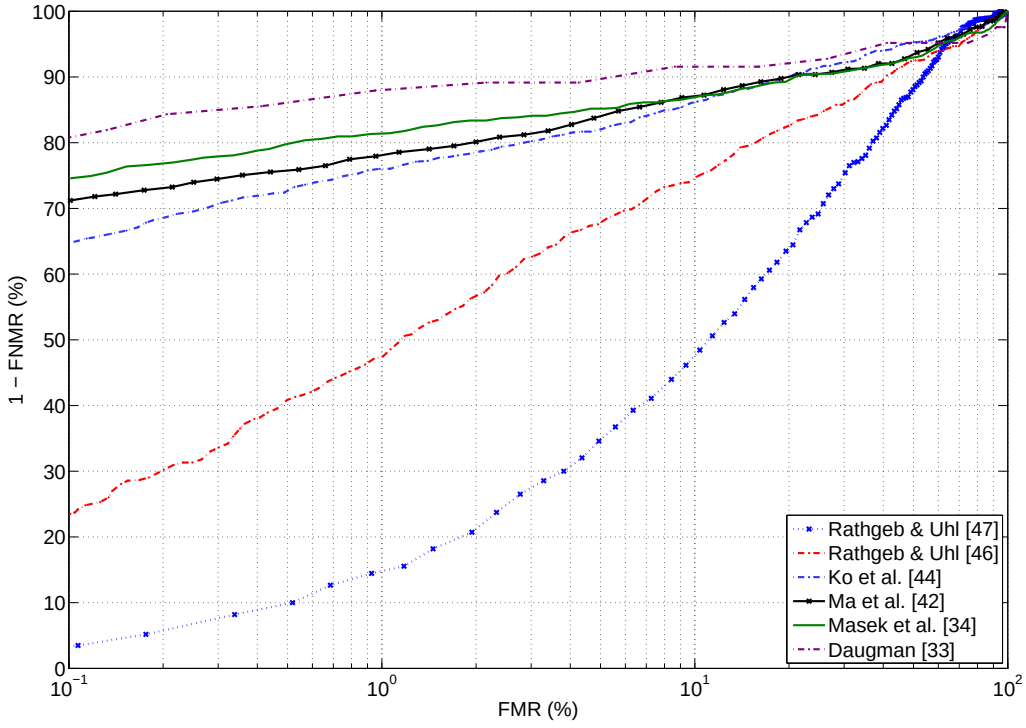

Figure 36: ROC Characteristics graph for iris images from Sony conventional camera.

Figure 35 shows the Receiver operating characteristic (ROC) for the performance

measured for Lytro light-field camera. The best performance is seen for the Daugman's 2D Gabor features and the worst performance is obtained for context based iris features. Figure 36 shows the corresponding ROC for the conventional camera (Sony DSC 750). The ROC shows the clear increase in $1-\mathrm{FNMR}$ at $\mathrm{FMR} = 10^{-1}$ for the light-field camera in Figure 35. Thus from the results given in this section, it has been experimentally verified that the light-field camera provides much higher accuracy in the visible spectrum iris recognition.

6.5 Focus Quality For Robust Segmentation

The pipeline of iris recognition system starts with the segmentation of the iris region after the capture. The segmentation plays a major role in the accuracy of the iris verification. Wrong segmentation of the iris region results in the wrong features and thus the rate of accurate verification decreases. Although, the study of segmentation accuracy is beyond the scope of this work, we throw some light on the importance of the focus for robust iris segmentation.

Figure 37(a)-(g) illustrates the segmentation for iris images at different focus for a single subject. The iris pattern is wrongly segmented for the iris in Figure 37(f) which is also observed to have very low focus. Bad focus quality thus results in the wrong segmentation. The corresponding normalized iris images are shown in the Figure 38. The block marked with red color in the image corresponds to the normalized image with inaccurate segmentation (Refer Fig 37(f))

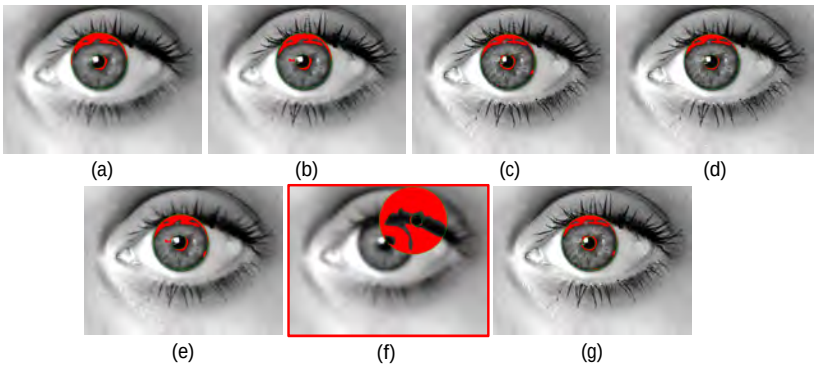

Figure 37: Segmentation for the different focus images. (a)-(g) Segmentation for iris image at different focus; (f) Bad segmentation for poor focus iris image

Thus the inaccurate segmentation of the iris image due to bad focus quality impacts the normalization and hence the iris recognition/verification. Care has to be taken during the acquisition to obtain good images with better focus in case of conventional camera. However, in the case of light-field camera, we can obtain all-in-focus image after the acquisition.

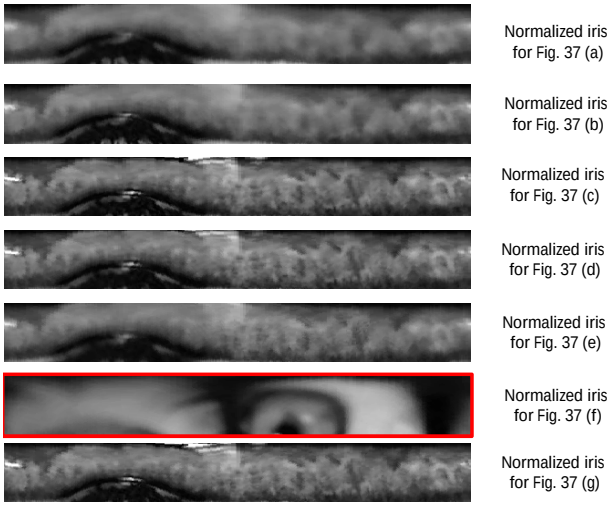

Figure 38: Normalized iris for different focus images corresponding to the iris in Figure 37

6.6 Focus Quality For Robust Recognition

The main motivation of this work lies in the focus-after-capture property of light-field imaging. Multiple depth images captured using the light-field camera can be fused to obtain a best-focus or all-in-focus image. Better focus for image capture results in the high texture information of the iris pattern. Higher texture information results in good number of edges and thus resulting in higher energy content. In previous works on light-field imaging by Raghavendra et al. [57], the sharpness of the image is measured using the wavelet energy decomposition. Deriving inspiration from their work, we propose to use the wavelet energy as a measure to quantify the focus of the normalized iris. In this work, we employ 'Haar' wavelet as the mother wavelet and decompose the image into 2 levels. Each level is measured for the energy component. The resulting sum value given by Equation 6.4 is a direct measure of the focus. The higher the energy, the higher is the focus measured.

Let $I(x, y)$ be the normalized iris image, the 2D DWT operation consists of two steps: filtering and downsampling using low-pass filter (L) and high pass filter (H) carried out on both rows and columns of $I(x, y)$. This procedure will result in four sub-images $I_{LL}(x, y)$, $I_{LH}(x, y)$, $I_{HL}(x, y)$ and $I_{HH}(x, y)$ where, $I_{LL}(x, y)$ is a smoothed image corresponding to the low-frequency band that represent the coarse approximation of the original image $I(x, y)$ and is termed as A_I. $I_{LH}(x, y)$, $I_{HL}(x, y)$ and $I_{HH}(x, y)$ represent the detailed sub-images corresponding to horizontal, vertical and diagonal directions of the image $I(x, y)$ and are termed as H_I, V_I and D_I. Given the DWT sub-images (horizontal, vertical and diagonal) corresponding to the normalized iris image $I(x, y)$, the wavelet energy for the sub-images are computed as below:

$$E_H = \sum_{x=1}^{R} \sum_{y=1}^{C} (H(x, y))^2 \tag{6.1}$$

$$E_V = \sum_{x=1}^{R} \sum_{y=1}^{C} (V(x,y))^2 \tag{6.2}$$

$$E_D = \sum_{x=1}^{R} \sum_{y=1}^{C} (D(x,y))^2 \tag{6.3}$$

where R and C correspond to rows and columns in the normalized iris image. The total energy of the normalized iris E_{Total} is given as:

$$E_{Total} = E_H + E_V + E_D \tag{6.4}$$

where H, V and D represent the horizontal, vertical and diagonal sub-images corresponding to the normalized iris image $I(x,y)$.

As the light-field camera provides us better focus, it is expected to provide higher values of energy with respect to the samples acquired from a conventional camera. Figure 39 illustrates the wavelet energy measured for the samples acquired from the conventional camera and the corresponding all-in-focus image for the same subject acquired using light-field camera. It can be clearly observed that light-field camera emerges a clear winner for providing best focus. Figure 39 also supports the obtained verification accuracy reported in the Table 4. The results indicate the usefulness of employing wavelet based energy measures to measure the focus quality of the iris image.

Figure 40 shows the focus measure for all the 420 samples of images acquired using light-field camera and conventional camera. The distribution clearly indicates the difference for each sample of iris acquired using both cameras. The focus for 99.76% of the images are higher in the light-field camera.

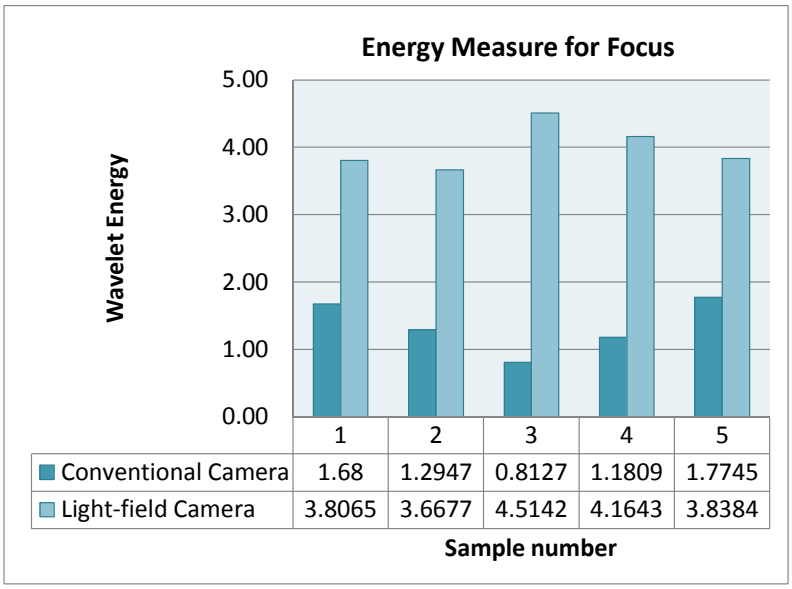

Figure 39: Focus measured using wavelet energy for light-field camera and conventional camera. Absolute energy measured can be seen under the horizontal axis of the graph.

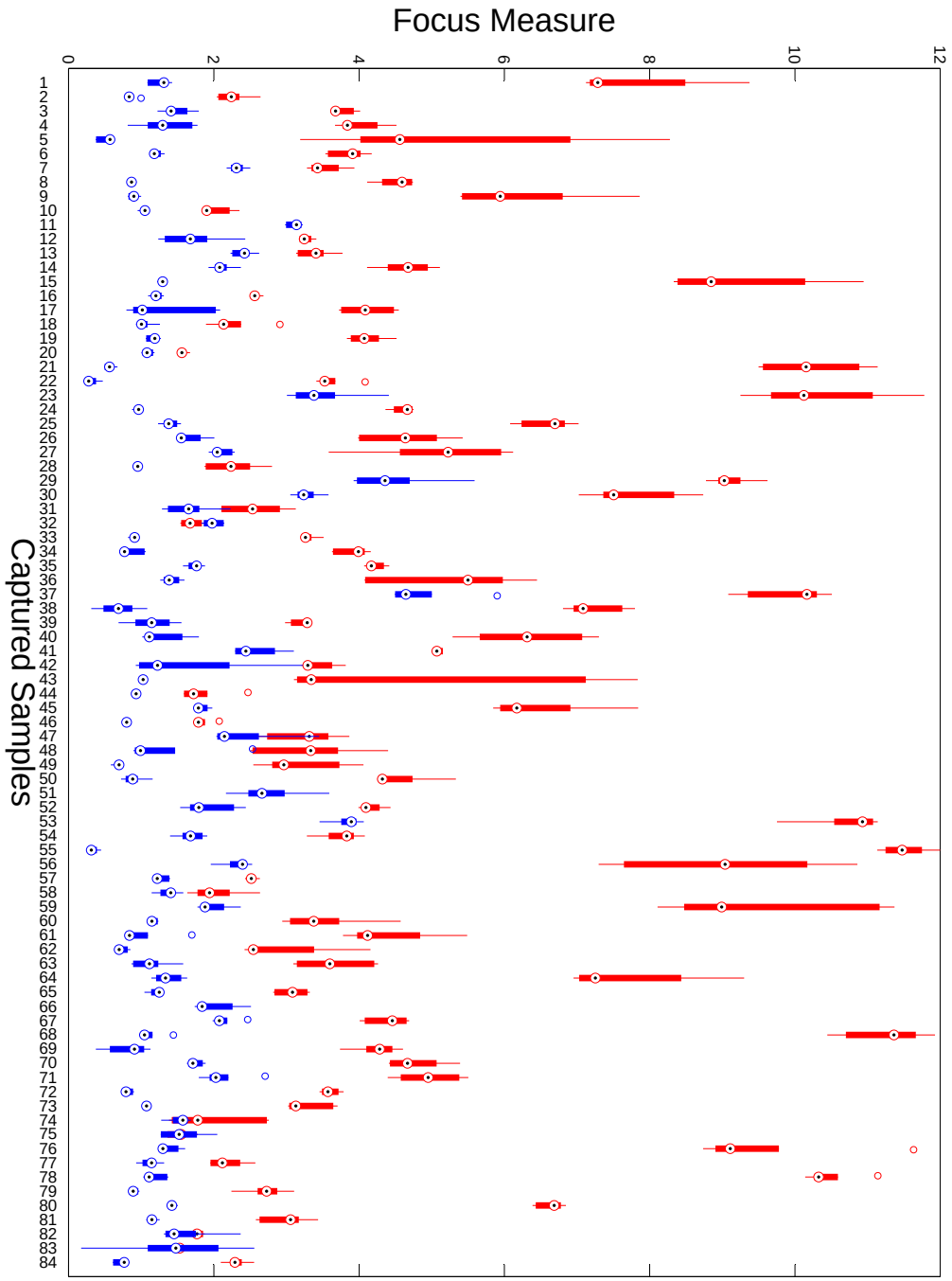

Figure 40: Focus distribution for conventional camera and light-field camera, Blue color corresponds to the focus measured for conventional camera and Red corresponds to light-field camera

6.7 Discussion

In this chapter, the experimental results for the GUCCID and GUCLID database was presented. The importance of focus in iris recognition was exemplified through various il-

lustrations. The experimental proof showing better performance for proposed scheme of using the light-field camera for iris recognition was demonstrated. This addresses the issue of out-of-focus in conventional iris capture systems under visible spectrum. The focus measure for all the samples employed in this experiment showed the clear distinction with respect to conventional camera. The performance scores for the light-field camera for all the 6 feature extraction schemes [33, 34, 42, 44, 46, 47] has shown promising results. It can thus be argued that higher focus values obtained for the light-field images has contributed to enhanced accuracy in recognition/verification.

7 Conclusions

This chapter presents the interpretation of obtained results with the conducted experiments. An analysis is presented with supporting arguments. Further, we also present the foreseeable research work and its impacts on the iris recognition for biometrics. This thesis aimed at answering two important questions:

1. Can the out-of-focus imaging present in visible spectrum iris recognition systems be addressed?
2. Can we adopt the existing imaging system to solve the issue of out-of-focus by extending the Depth-of-Field(DOF)?

It can be evidently seen from the experiments that out-of-focus issue in visible spectrum iris imaging can be addressed using the new generation of sensors based on light-field principle. The depth-of-field can be effectively extended with a single exposure acquisition using light-field camera. This work has utilized the existing sensor to address the limited depth-of-field to obtain sharp iris images.

7.1 Conclusions And Remarks

The main motivation of this work was to address the out-of-focus imaging in the conventional iris imaging systems in visible spectrum. We have explored the strength of the light-field technology for the benefit of iris imaging. Multiple depth images obtained from single exposure is fused to obtain a all-in-focus image. The all-in-focus image was employed for iris recognition to solve the problem of out-of-focus. The problem of limited depth-of-field for iris imaging has been addressed using light-field camera. In this work, we have proposed a novel scheme with the new generation of light-field sensors. We have employed the Lytro light-field camera to experimentally support our proposed scheme. The whole experiment was conducted on 84 unique iris with 5 samples for each iris which were captured using conventional camera and light-field camera. This work has resulted in the creation of unique iris database captured with conventional camera and light-field camera with 420 sample images along with 3387 depth images. The light-field iris database is the first and unique databases which will be made available to the research community in near future.

As compared to the existing methods [33, 48, 49, 50, 51] to address the out-of-focus imaging in iris recognition, the proposed scheme offers the following advantages:

1. Iris image is acquired in single exposure and thus avoids multiple acquisitions until satisfactory focus is obtained.
2. Iris image does not need multiple frames of capture unlike in video based methods and thus is computationally efficient.
3. Near zero shutter lag of the light-field camera efficiently reduces the time required for the iris capture.

4. The device is priced at low cost and thus the proposed scheme is cost-effective.

We have employed existing methods to obtain an all-in-focus image from multiple-focus images for the experiment. The outcomes of the experiment have shown the success of the proposed scheme. The comparison of the performance of light-field (all-in-focus) iris imaging with conventional iris imaging favours our argument for the proposed scheme. All-in-focus images obtained from the light-field camera reported an EER of 3.61% with 2D Gabor features proposed by Daugman [33] (Refer Table 4), while the highest rate of EER (worst performance) has been demonstrated for the context based iris features[47] for conventional iris images with 27.38% EER.

7.2 Contributions

This work has contributed in three important aspects for iris recognition:

1. A novel way to address out-of-focus iris imaging has been proposed and validated experimentally.
2. Two new iris databases are created out of this work. An unique light-field iris database shall be made available to research community in near future.
3. Wavelet based energy measure has been proposed to quantify the focus of iris image. The proposed focus measure has been experimentally supported.

7.3 Foreseeable Research Work

As this thesis work proposes a new scheme for iris recognition, some of the possible future works are identified and listed in this section.

7.3.1 3D Iris

Due to the availability of multiple depth/focus images, 3D view of the iris can be constructed. Due to spherical nature of the eye-balls, the imaging deformities introduced in planar imaging can be avoided. Another interesting aspect of 3D view of the iris is to solve the issue of spoofing and detect the liveliness of the subject.

7.3.2 All-in-focus v/s Refocus

This work has considered all-in-focus images for the recognition/verification. As the focus of regions vary, it will be interesting to use the image with highest focus measured employing the proposed method of wavelet energy in the iris region. The whole idea for this work has to follow the method of back-projecting the obtained radius from all-in-focus image to rest of the depth/focus images. Normalizing each depth image from the segmented iris and measuring the energy might improve the accuracy. This argument is put forward because of the fact that creation of all-in-focus image may trade-off certain details from the depth/focus image and these details might include the iris region as well.

7.3.3 Encoder Change

The encoder used by Lytro light-field camera does not produce optimum quality of the output. This introduces certain amount of artifacts in the features obtained from iris image. These artifacts impact the performance of the recognition/verification in terms of accuracy. The changes in the encoder architecture in future release of the employed light-field camera is projected to improve the reported accuracy in iris recognition.

7.3.4 Spatial Resolution

The greatest drawback of the light-field camera employed in this work lies in the effective spatial resolution of the camera. The conventional camera used in this work has an effective resolution of 7.2 megapixels and the light-field camera has a resolution of 1.2 megapixels. Lower resolution of the camera leads to the decreased details in the texture pattern. A camera with higher spatial resolution is projected to provide higher accuracy with respect to recognition or verification accuracy.

7.3.5 Influence Of Parameters

The iris database is created to resemble the real-life surveillance scenario of at-a-distance iris capture in visible spectrum. The imaging devices were operated in automatic mode. A detailed study on varying the individual parameters of the imaging device for iris image acquisition can be conducted to validate the influence on the quality of the images in the database. Another aspect of study is to quantify and differentiate the imaging errors and the errors due to noise in images. Fusing the images to obtain all-in-focus image can potentially introduce some artifacts. A detailed study on these factors was beyond the scope of the work and is recommended in future work to provide supporting arguments for the proposed scheme.

Bibliography

[1] Levoy, M., Ng, R., Adams, A., Footer, M., & Horowitz, M. 2006. Light field microscopy. In *ACM Transactions on Graphics (TOG)*, volume 25, 924–934. ACM.

[2] Adelson, E. H. & Bergen, J. R. 1991. The plenoptic function and the elements of early vision. In *Computational Models of Visual Processing*, 3–20. MIT Press.

[3] Adelson, E. & Wang, J. 1992. Single lens stereo with a plenoptic camera. *IEEE Transactions on Pattern Analysis and Machine Intelligence*, 14(2), 99–106.

[4] McMillan, L. & Bishop, G. 1995. Plenoptic modeling: An image-based rendering system. In *Proceedings of the 22nd annual conference on Computer graphics and interactive techniques*, 39–46. ACM.

[5] Levoy, M. & Hanrahan, P. 1996. Light field rendering. In *Proceedings of the 23rd annual conference on Computer graphics and interactive techniques*, 31–42. ACM.

[6] Ng, R., Levoy, M., Brédif, M., Duval, G., Horowitz, M., & Hanrahan, P. 2005. Light field photography with a hand-held plenoptic camera. *Computer Science Technical Report CSTR*, 2.

[7] Vaish, V., Wilburn, B., Joshi, N., & Levoy, M. june-2 july 2004. Using plane + parallax for calibrating dense camera arrays. In *Computer Vision and Pattern Recognition, 2004. CVPR 2004. Proceedings of the 2004 IEEE Computer Society Conference on*, volume 1, I–2 – I–9 Vol.1.

[8] Isaksen, A., McMillan, L., & Gortler, S. 2000. Dynamically reparameterized light fields. In *Proceedings of the 27th annual conference on Computer graphics and interactive techniques*, 297–306. ACM Press/Addison-Wesley Publishing Co.

[9] Favaro, P. & Soatto, S. june 2003. Seeing beyond occlusions (and other marvels of a finite lens aperture). In *Computer Vision and Pattern Recognition, 2003. Proceedings. 2003 IEEE Computer Society Conference on*, volume 2, II–579 – II–586 vol.2.

[10] Fife, K., El Gamal, A., & Wong, H. 2006. A 3d multi-aperture image sensor architecture. In *Custom Integrated Circuits Conference, 2006. CICC'06. IEEE*, 281–284. IEEE.

[11] Veeraraghavan, A., Raskar, R., Agrawal, A., Mohan, A., & Tumblin, J. 2007. Dappled photography: Mask enhanced cameras for heterodyned light fields and coded aperture refocusing. *ACM Transactions on Graphics*, 26(3), 69.

[12] Liang, C., Liu, G., & Chen, H. 2007. Light field acquisition using programmable aperture camera. In *Image Processing, 2007. ICIP 2007. IEEE International Conference on*, volume 5, V–233. IEEE.

[13] Raytrix GmbH. "`http://www.raytrix.de/`".

[14] Lytro Inc. ""http://www.lytro.com/".

[15] Harris, M. 2012. Focusing on everything. *Spectrum, IEEE*, 49(5), 44–50.

[16] ISO/IEC TC JTC1 SC37 Biometrics. *ISO/IEC 19795-1:2006. Information Technology – Biometric Performance Testing and Reporting – Part 1: Principles and Framework*. International Organization for Standardization and International Electrotechnical Committee, March 2006.

[17] Adler, F. 1965. Physiology of the eye, mosby, st. *Louis, Mo*.

[18] Kronfeld, P. 1962. Gross anatomy and embryology of the eye. *The eye*, 1, 1–66.

[19] Chedekel, M. 1995. Photophysics and photochemistry of melanin. *Melanin: Its Role in Human Photoprotection*, 11–23.

[20] Daugman, J. 2004. How iris recognition works. *Circuits and Systems for Video Technology, IEEE Transactions on*, 14(1), 21–30.

[21] Rathgeb, C., Uhl, A., & Wild, P. 2012. *Iris Recognition: From Segmentation to Template Security*. Number 59 in Advances in Information Security. Springer-Verlag, 1st edition.

[22] Adini, Y., Moses, Y., & Ullman, S. 1997. Face recognition: The problem of compensating for changes in illumination direction. *Pattern Analysis and Machine Intelligence, IEEE Transactions on*, 19(7), 721–732.

[23] Uniqueness, U. E. 2010. Collecting iris biometrics for the unique id mission. *UIDAI (undated)*.

[24] UIDAI, G. Biometrics design standards for uid applications.

[25] Atos Origin. 2005. Uk passport service biometrics enrolment trial. *Report. Retrieved April*, 15, 2009.

[26] Proença, H. 2013. Iris recognition in the visible wavelength. In *Handbook of Iris Recognition*, 151–169. Springer.

[27] Lefevre, T., Dorizzi, B., Garcia-Salicetti, S., Lemperiere, N., & Belardi, S. 2013. Effective elliptic fitting for iris normalization. *Computer Vision and Image Understanding*.

[28] Sutra, G., Dorizzi, B., Garcia-Salicetti, S., & Othman, N. 2012. A biometric reference system for iris, osiris version 4.1.

[29] Gonzalez, R. C., Woods, R. E., & Eddins, S. L. 2009. *Digital image processing using MATLAB*, volume 2. Gatesmark Publishing Tennessee.

[30] Wildes, R. P., Asmuth, J. C., Green, G. L., Hsu, S. C., Kolczynski, R. J., Matey, J., & McBride, S. E. 1994. A system for automated iris recognition. In *Applications of Computer Vision, 1994., Proceedings of the Second IEEE Workshop on*, 121–128. IEEE.

[31] Kong, W. & Zhang, D. 2001. Accurate iris segmentation based on novel reflection and eyelash detection model. In *Intelligent Multimedia, Video and Speech Processing, 2001. Proceedings of 2001 International Symposium on*, 263–266. IEEE.

[32] Tisse, C.-L., Martin, L., Torres, L., & Robert, M. 2002. Person identification technique using human iris recognition. In *Proc. of Vision Interface*. Citeseer.

[33] Daugman, J. 2002. How iris recognition works. In *Image Processing. 2002. Proceedings. 2002 International Conference on*, volume 1, I–33. IEEE.

[34] Masek, L. Recognition of human iris patterns for biometric identification. Master's thesis, University of Western Australia, 2003.

[35] Kittler, M. J. *Reconnaissance des personnes par l'iris en mode dégradé*. PhD thesis, Institut National des Télécommunications, 2007.

[36] Daugman, J. 2007. New methods in iris recognition. *Systems, Man, and Cybernetics, Part B: Cybernetics, IEEE Transactions on*, 37(5), 1167–1175.

[37] Pundlik, S. J., Woodard, D. L., & Birchfield, S. T. 2008. Non-ideal iris segmentation using graph cuts. In *Computer Vision and Pattern Recognition Workshops, 2008. CVPRW'08. IEEE Computer Society Conference on*, 1–6. IEEE.

[38] Hollingsworth, K., Bowyer, K. W., & Flynn, P. J. 2009. Pupil dilation degrades iris biometric performance. *Computer Vision and Image Understanding*, 113(1), 150–157.

[39] Sutra, G., Garcia-Salicetti, S., & Dorizzi, B. 2012. The viterbi algorithm at different resolutions for enhanced iris segmentation. In *Biometrics (ICB), 2012 5th IAPR International Conference on*, 310–316. IEEE.

[40] Oppenheim, A. V. & Lim, J. S. 1981. The importance of phase in signals. *Proceedings of the IEEE*, 69(5), 529–541.

[41] Field, D. J. et al. 1987. Relations between the statistics of natural images and the response properties of cortical cells. *J. Opt. Soc. Am. A*, 4(12), 2379–2394.

[42] Ma, L., Tan, T., Wang, Y., & Zhang, D. 2003. Personal identification based on iris texture analysis. *Pattern Analysis and Machine Intelligence, IEEE Transactions on*, 25(12), 1519–1533.

[43] Daugman, J. 2001. Statistical richness of visual phase information: update on recognizing persons by iris patterns. *International Journal of Computer Vision*, 45(1), 25–38.

[44] Ko, J.-G., Gil, Y.-H., Yoo, J.-H., & Chung, K.-I. 2007. A novel and efficient feature extraction method for iris recognition. *ETRI journal*, 29(3), 399–401.

[45] Taylor, W. A. 2000. Change-point analysis: a powerful new tool for detecting changes. *preprint, available as http://www. variation. com/cpa/tech/changepoint. html*.

[46] Rathgeb, C. & Uhl, A. 2010. Secure iris recognition based on local intensity variations. In *Image Analysis and Recognition*, 266–275. Springer.

[47] Rathgeb, C. & Uhl, A. 2009. Context-based texture analysis for secure revocable iris-biometric key generation. In *Crime Detection and Prevention (ICDP 2009), 3rd International Conference on*, 1–6. IET.

[48] Narayanswamy, R., Silveira, P. E., Setty, H., Pauca, V. P., & van der Gracht, J. 2005. Extended depth-of-field iris recognition system for a workstation environment. In *Defense and Security*, 41–50. International Society for Optics and Photonics.

[49] Boddeti, N. & Kumar, B. 2008. Extended depth of field iris recognition with correlation filters. In *Biometrics: Theory, Applications and Systems, 2008. BTAS 2008. 2nd IEEE International Conference on*, 1–8. IEEE.

[50] Park, K. R. & Kim, J. 2005. A real-time focusing algorithm for iris recognition camera. *Systems, Man, and Cybernetics, Part C: Applications and Reviews, IEEE Transactions on*, 35(3), 441–444.

[51] Tankasala, S. P., Gottemukkula, V., Saripalle, S. K., Nalamati, V. G., Derakhshani, R., Pasula, R., & Ross, A. 2012. A video-based hyper-focal imaging method for iris recognition in the visible spectrum. In *Homeland Security (HST), 2012 IEEE Conference on Technologies for*, 214–219. IEEE.

[52] Zhang, G. H. & Salganicoff, M. September 14 1999. Method of measuring the focus of close-up images of eyes. US Patent 5,953,440.

[53] Note on CASIA-Iris v.3. "`http://www.cbsr.ia.ac.cn/IrisDatabase.htm`".

[54] Proenca, H., Filipe, S., Santos, R., Oliveira, J., & Alexandre, L. A. 2010. The ubiris. v2: A database of visible wavelength iris images captured on-the-move and at-a-distance. *Pattern Analysis and Machine Intelligence, IEEE Transactions on*, 32(8), 1529–1535.

[55] Phillips, P. J., Bowyer, K. W., Flynn, P. J., Liu, X., & Scruggs, W. T. 2008. The iris challenge evaluation 2005. In *Biometrics: Theory, Applications and Systems, 2008. BTAS 2008. 2nd IEEE International Conference on*, 1–8. IEEE.

[56] Dobeš, M. & Machala, L. Upol iris database. `http://www.inf.upol.cz/iris/`.

[57] R Raghavendra, Kiran B Raja, Yang, B., & Busch, C. 2013. A novel image fusion scheme for robust multiple face recognition with light-field camera. In *to appear, Information Fusion (FUSION), 2013 16th International Conference on*. IEEE. (To appear).

A Additional Experiments

Additional set of experiments have been conducted on the acquired iris image database. Normalized iris images are chosen based on the proposed focus measure. The focus is a direct measure of the wavelet energy which implies that higher energy corresponds to better focus.

Let $I(x,y)$ be the normalized iris image, the 2D DWT operation consists of two steps: filtering and downsampling using low-pass filter (L) and high-pass filter (H) carried out on both rows and columns of $I(x,y)$. This procedure results in four sub-images $I_{LL}(x,y)$, $I_{LH}(x,y)$, $I_{HL}(x,y)$ and $I_{HH}(x,y)$ where, $I_{LL}(x,y)$ is smoothed image corresponding to the low-frequency band that represent the coarse approximation of the original image $I(x,y)$ and termed as A_I. $I_{LH}(x,y)$, $I_{HL}(x,y)$ and $I_{HH}(x,y)$ represents the detailed sub-images corresponding to horizontal, vertical and diagonal directions of the image $I(x,y)$ and termed as H_I, V_I and D_I. Given the DWT sub-images (horizontal, vertical and diagonal) corresponding to the normalized iris image $I(x,y)$, the wavelet energy for the sub-images are computed as:

$$E_H = \sum_{x=1}^{R}\sum_{y=1}^{C}(H_I(x,y))^2 \tag{A.1}$$

$$E_V = \sum_{x=1}^{R}\sum_{y=1}^{C}(V_I(x,y))^2 \tag{A.2}$$

$$E_D = \sum_{x=1}^{R}\sum_{y=1}^{C}(D_I(x,y))^2 \tag{A.3}$$

where, R and C correspond to rows and columns in the normalized iris image.

$$E_{Total} = E_H + E_V + E_D \tag{A.4}$$

H, V and D represents the horizontal, vertical and diagonal sub-images for the normalized iris image $I(x,y)$. Considering n normalized iris images from single exposure capture representing different depth, the best focused energy is obtained according to the maximum energy.

Let $\{I_1(x,y), I_2(x,y) \ldots I_n(x,y)\}$ represent n normalized iris images. From the set of computed energy of each normalized image according to Equation A.4, the best focus normalized iris image given as $I_{bf}(x,y)$ corresponds to image with highest energy E_{max} obtained as:

$$E_{max} = max\{E_{1_{Total}}, E_{2_{Total}} \ldots E_{n_{Total}}\}. \tag{A.5}$$

$$I_{bf}(x,y) = I_i(x,y) \quad \text{if} \quad E_{i\ Total} = E_{max} \tag{A.6}$$
$$\text{for } i = 1,2,...n$$

The best-focused iris image $I_{bf}(x, y)$ is used for feature extraction and feature comparison. Table 5 provides the quantitative score of iris recognition results with best focused depth images. Receiver operating characteristic (ROC) graphs for best focused iris images from light-field camera are presented in Figure 41.

Table 5: Quantitative results obtained from various schemes for best-focused iris images.

Feature Extraction	EER (%)	
	Light-field Camera	Conventional camera
Rathgeb & Uhl [47]	26.92	27.38
Rathgeb & Uhl [46]	11.84	18.24
Ko et al. [44]	5.95	12.55
Ma et al. [42]	5.78	12.07
Masek et al. [34]	5.26	12.44
Daugman [33]	2.38	8.53

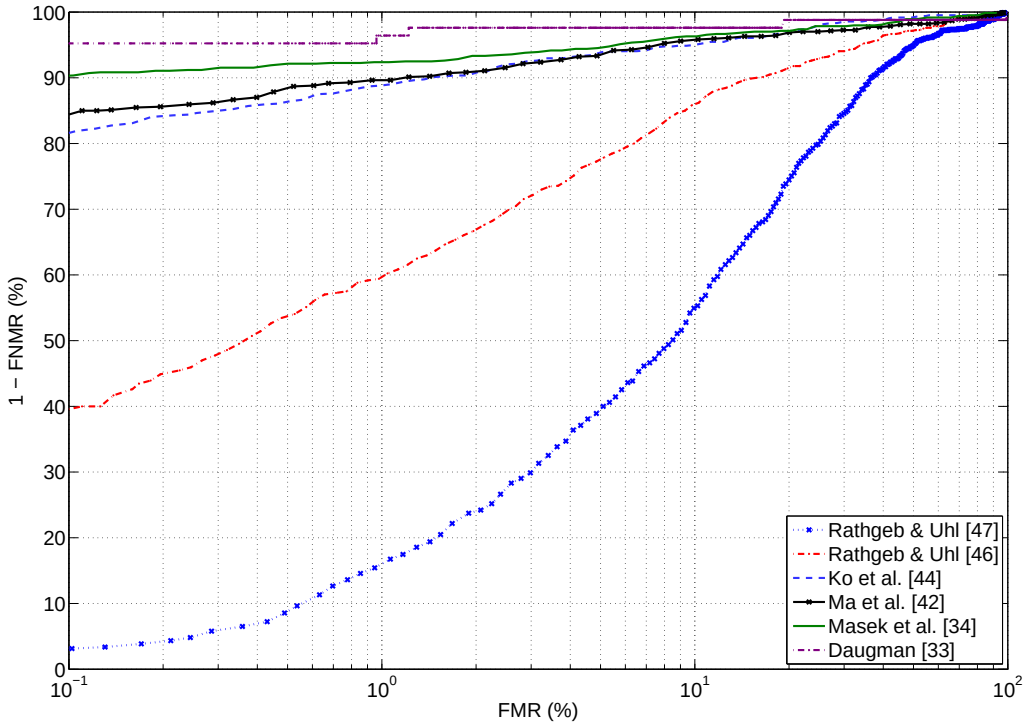

Figure 41: Receiving Operator Characteristic graph for best-focused iris images from light-field camera.

B Robust Iris Recognition Using Light-field Camera

A scientific paper disseminating the results of using light-field cameras for iris recognition in visible spectrum is presented in this section. This paper has been accepted for publication in CVCS2013 (`http://colourlab.no/events/cvcs2013`) and shall be published in IEEE conference proceedings of CVCS2013, Gjøvik, Norway.

ROBUST IRIS RECOGNITION USING LIGHT-FIELD CAMERA

Kiran B. Raja, R. Raghavendra, Faouzi Alaya Cheikh, Bian Yang, Christoph Busch

Gjøvik University College, Gjøvik, Norway
kiran.raja@hig.no, raghavendra.ramachandra@hig.no, faouzi.cheikh@hig.no
bian.yang@hig.no, christoph.busch@hig.no

ABSTRACT

Iris is one of the preferred biometric modalities. Nevertheless, the focus of iris image has to be good enough to achieve good recognition performance. Traditional iris imaging devices in the visible spectrum suffer from limited depth-of-field which results in out-of-focus iris images. The acquisition of iris image is thus repeated until a satisfactory focus is obtained or the image is post-processed to improve the visibility of texture pattern. Bad focused images obtained due to non-optimal focus degrade the identification rate. In this work, we propose a novel scheme to capture high quality iris samples by exploring new sensors based on light-field technology to address the limited depth-of-field exhibited by the conventional iris sensors. The idea stems out from the availability of multiple depth/focus images in a single exposure. We propose to use the best-focused iris image from the set of depth images rendered by the Light-field Camera (LFC). We further evaluate the proposed scheme experimentally with a unique and newly acquired iris database simulating the real-life scenario.

Index Terms— Biometrics, Iris recognition, Light-field camera, out-of-focus iris.

I. INTRODUCTION

The human iris is defined as a thin circular diaphragm lying between the cornea and the lens in the eye [1]. Iris is one of the organs present internally in human body but also visible externally when the eye-lids are open. The iris is known to develop in the third month of gestation and prominent structures resulting in the patterns are mostly complete by eighth month [18]. It contains rich amount of texture and unique structures like furrows, freckles, crypts, and coronas [1]. Color of the iris is known to vary individually for each person. The color is related to density of melanin pigment in the anterior layer and stroma [19] in iris. The presence of lower amount of melanin pigment in iris results in light colored iris and the higher amount results in darker iris. Light colored iris allows the penetration of long-wavelength light and usually scatters shorter wavelength light [2]. One important aspect to consider is the epigenetic nature of iris patterns. This results in unique, completely independent and uncorrelated iris patterns for an individual and even for identical twins. Biometric features such as face or fingerprint are always at the risk of being changed due to various factors. The performance of the recognition system depends largely on the change in facial expressions based on the social factors and also throws in challenges in recognition with varied illumination, age and pose [3]. Another well known biometric modality is fingerprint. Any intentional or unintentional scars or cuts on the fingerprint may introduce false recognition or rejection of authentic subjects. Fake fingerprint attack has to be considered for a secure biometric recognition. These factors influence the intra-class variability to larger extent and thereby make the inter-class variability lower. Lower inter-class variability leads to challenges in accurate recognition. Thus, iris provides two unique biometric identities for any single person with a high level of identification confidence. Human iris is also one of the most distinctive features for each individual and is thus used for robust biometric recognition. Owing to the robust level of identity protection it provides, iris recognition is unparalleled by any other biometric feature. Iris biometric feature is not prone to the vast changes or morphing over the period of lifetime.

To capture the iris pattern presented by the dark pigmented iris, traditional methods have employed the Near-Infra-Red illumination in the range of $700 - 900\ nm$. Atos Origin [4] has reported that stop-and-stare strategy followed by many iris recognition systems to acquire good quality images in the Near-Infra-Red region remains a major hurdle in deploying the iris-based biometrics in large scale for faster identification/recognition. Many of the currently deployed systems impose constraints on the subjects and acquisition environment. A subject is expected to stand close to the imaging device and co-operatively look into the camera under NIR illumination to assure good quality images. To achieve a good signal-to-noise ratio in the sensor and to capture images with highly discriminating iris features, high illumination is required [5]. This becomes non-acceptable for acquisitions under at-a-distance or on-the-move scenarios because of the amount of light required for the process. To broaden the scope of iris recognition in real-life at-a-distance and on-the-move surveillance scenarios, we have focused our work on visible spectrum iris recognition.

The focus of the imaging device is important for the quality of images in iris recognition systems. One of the key quality challenges in iris imaging is due to out-of-focus images. Previous works have shown the relation of the focus to image quality [6], [7]. The problem with most of the conventional imaging system is that they have limited depth-of-field which does not allow improvement in the focus after acquisition. The subject is thus constrained in right depth-of-field plane until good focus images are acquired.

Various approaches to address the problem of focus have been devised. Narayanswamy et al. [8] and Boddeti and Kumar [9] have explored the wavefront coded imaging for iris recognition systems. The key idea in their approach is to improve the overall sharpness of the image using wavefront coding. Park and Kim [10] used the spectral-reflection from the IR-LED illuminator as a feedback information to set the focus and zoom. Daugman [33] measured the power in 2D Fourier spectrum to assess the image's focus quality. More recently, Tankasala et al. [11] have proposed video based hyper-focal imaging. The video frames are captured under various focus for a specified duration. The captured frames under different focus are fused to obtain improved focus image for iris recognition. Extending the depth-of-field results in the decreased dynamic range and low SNR for the obtained images. Furthermore, video based methods use sequence of frames which demand high amount of memory and computation along with the need for more acquisition time.

In this work, we propose a novel scheme to address the issue of out-of-focus iris image capture by employing light-field (or plenoptic) imaging techniques. We have adopted first available consumer Light-Field Camera (LFC) by Lytro Inc[12] for iris imaging. The plenoptic/lightfield cameras are constructed by inserting a micro-lens array [13] or a pin-hole array or masks [14] between the sensor and main lens of camera. The presence of these micro-lenses (or array of pin-holes or masks) measures the total amount of light deposited on the sensor and the direction of each ray of the incoming light. By re-sorting the measured rays of light with respect to their point of termination, a number of images focused at different depths can be obtained. Light-field camera offers the following key advantages: (1) Generates images at different focus (or depth) in single exposure; (2) It is a low cost device; (3) Portable and hand-held; (4) Provides real-time exposure with no shutter lag. With the number of advantages provided by the light-field camera, multiple depth or focus images obtained can be exploited to: (1) Obtain refocus images; (2) Obtain all-in-focus images; (3) Estimate depth; (4) Obtain synthetic aperture image.

In this work, we have exploited multiple depth images to obtain the best focused iris image to address the issue of out-of-focus image. We then employ the best focused iris image to perform the recognition. We perform the wavelet energy based focus measure mentioned in [15] to select the best focus image from the multi-focus images.

In the rest of the paper, Section II presents the new database acquired during the experiments, Section III presents the details on proposed scheme. Section V provides the details of experimental results and the concluding remarks.

II. LIGHT-FIELD IRIS DATABASE

In the context of non-availability of any light-field iris database, an unique light-field iris database is constructed. In order to perform the baseline comparison with the conventional iris imaging systems, we have also constructed iris database acquired from the conventional 2D camera. We have employed Lytro light-field camera and conventional (Sony DSC S750) camera. Lytro light-field camera has a resolution of 11 Megarays and an effective spatial resolution of 1.2 megapixels while the conventional camera has an effective spatial resolution of 7.2 megapixels. The conventional camera was operated with auto-focus over the iris region. The camera was mounted on the tripod at a distance of 10-15 inches from the subject and the images were acquired in an interval of around 30 seconds. The iris databases consists of 84 unique iris obtained from 42 different subjects. Both the databases consist of 5 samples for each iris image making it a database with 420 iris samples. The whole database was captured over a period of 25 days. The subject set consists of 22 male and 20 female subjects giving a distribution of 70 light-coloured iris, 10 amber-coloured iris and 4 dark coloured iris.

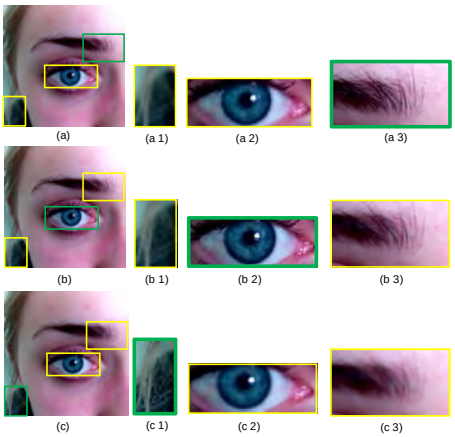

Fig. 1. Illustration of varied focus.

Each image captured from the light-field camera results in a raw file with set of images. Each of these images correspond to different depth planes and the focus of the image varies in an individual image. Figure 1 illustrates the varied focus over the image in different depth images. Figure 1(a), (b) and (c) depict the depth image. It can be observed that the image has sharp focus in the region shown by (a 3), (b 2) and (c 1) while other regions are not focused. In order to perform

the analysis, we select the best focused image corresponding to iris region from multiple focus image based on wavelet energy [15].

The information about the sharp regions in an image is stored in the metadata file accompanying the image. We have constructed the best-focused light-field iris image database using the depth images. The light-field iris image database has a total of 3387 depth images. The best focused iris image is obtained based on the focus measured using the wavelet based energy. Details of this technique is presented in the Section III-B.

III. PROPOSED SCHEME

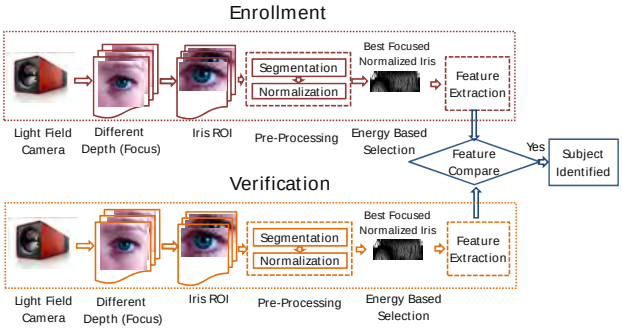

Fig. 2. Proposed Iris Recognition Scheme

The proposed scheme is illustrated in the Figure 2. As with any other biometric recognition, the proposed scheme has two components : enrollment and verification. In the enrollment, iris images are captured using the light-field camera under the visible spectrum illumination. To obtain the accurate segmentation and avoid false iris region detection, we propose to use the region-of-interest(ROI) consisting of the eye only. To extract ROI, the image is transformed to YC_bC_r color space and the difference between the C_b and C_r channel is computed. The obtained image is binarized using Otsu's threshold [16] and the largest area in the central region is identified as the eye. Extended bounding box is computed to have complete iris pattern. The extracted ROI is then segmented. Figure 3 illustrates the necessity to extract the ROI to obtain accurate segmentation of iris. It can be observed from the figure that false iris detection is avoided with the ROI extracted image.

III-A. Segmentation and Normalization

In this work, OSIRIS v4.1 [17] is employed for segmentation to the obtain the clear boundaries between the pupil and iris region. The choice of using OSIRIS is based on the previous works demonstrating its superior performance in segmentation [18]. The segmented iris in the image is transformed into a normalized image with doubly dimensionless pseudopolar coordinate system [19]. Further, as light-field camera provides multiple depth images, we propose to

Fig. 3. Necessity for ROI extraction; (a) Captured eye image; (b) False iris segmentation; (c) Accurate iris segmentation with ROI image.

obtain the best focused normalized iris image for recognition process. Distinct iris features are obtained using the state-of-art feature extraction techniques. The extracted features are compared for recognition using the Hamming distance measure proposed by Daugman[19].

III-B. Best Focused Iris Image Selection

The main motivation of this work is to obtain the best focused image after capture. Of all the multiple depth-images obtained, the image having the highest energy is considered for the recognition. Better focus for image capture results in high texture information in the iris pattern. Higher texture information results in good number of edges and thus resulting in higher energy content. In previous works on light-field imaging by Raghavendra et al. [15], the sharpness of the image was measured using the wavelet energy decomposition. Deriving inspiration from their work, we propose to use the wavelet energy as a measure to quantify the focus of the normalized iris. We employ "Haar" wavelet as the mother wavelet and decompose the image into 2 levels. Each level is measured individually for the energy component. The resulting sum value given by Equation 4 is a direct measure of the focus. The higher the energy, the higher the focus measured is.

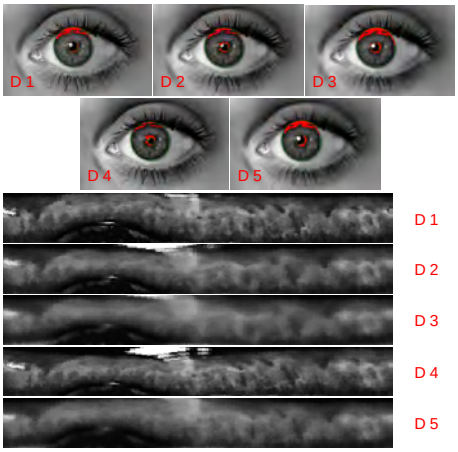

Fig. 4. Multiple depth images in a single exposure. Depth 1-5 are represented as D 1 - D 5.

Let $I(x,y)$ be the normalized iris image, the 2D DWT operation consists of two steps: filtering and downsampling using low-pass filter (L) and high-pass filter (H) carried out on both rows and columns of $I(x,y)$. This procedure results in four sub-images $I_{LL}(x,y)$, $I_{LH}(x,y)$, $I_{HL}(x,y)$ and $I_{HH}(x,y)$ where, $I_{LL}(x,y)$ is smoothed image corresponding to the low-frequency band that represent the coarse approximation of the original image $I(x,y)$ and termed as A_I. $I_{LH}(x,y)$, $I_{HL}(x,y)$ and $I_{HH}(x,y)$ represents the detailed sub-images corresponding to horizontal, vertical and diagonal directions of the image $I(x,y)$ and termed as H_I, V_I and D_I. Given the DWT sub-images (horizontal, vertical and diagonal) corresponding to the normalized iris image $I(x,y)$, the wavelet energy for the sub-images are computed as:

$$E_H = \sum_{x=1}^{R}\sum_{y=1}^{C}(H_I(x,y))^2 \tag{1}$$

$$E_V = \sum_{x=1}^{R}\sum_{y=1}^{C}(V_I(x,y))^2 \tag{2}$$

$$E_D = \sum_{x=1}^{R}\sum_{y=1}^{C}(D_I(x,y))^2 \tag{3}$$

where, R and C correspond to rows and columns in the normalized iris image.

$$E_{Total} = E_H + E_V + E_D \tag{4}$$

H, V and D represents the horizontal, vertical and diagonal sub-images for the normalized iris image $I(x,y)$. Considering n normalized iris images from single exposure capture representing different depth, the best focused energy is obtained according to the maximum energy.

Let $\{I_1(x,y), I_2(x,y) \ldots I_n(x,y)\}$ represent n normalized iris images. From the set of computed energy of each normalized image according to Equation 4, the best focus normalized iris image given as $I_{bf}(x,y)$ corresponds to image with highest energy E_{max} obtained as:

$$E_{max} = max\left\{E_{1_{Total}}, E_{2_{Total}} \ldots E_{n_{Total}}\right\}. \tag{5}$$

$$I_{bf}(x,y) = I_i(x,y) \quad \text{if} \quad E_{i\ Total} = E_{max} \tag{6}$$

$$for\ i = 1, 2, ...n$$

The best-focused iris image $I_{bf}(x,y)$ is used for feature extraction.

Figure 5 shows the measured focus in-terms of the wavelet energy for iris samples acquired for a single subject using light-field and conventional cameras. The best-focused light-field images have higher energy and thus higher focus compared to the conventional iris images. Figure 6 shows the energy measured for various depth images for the normalized iris captured from light-field camera in single exposure. The depth represented by D 4 gives highest energy and thus is chosen to carry out the performance evaluation.

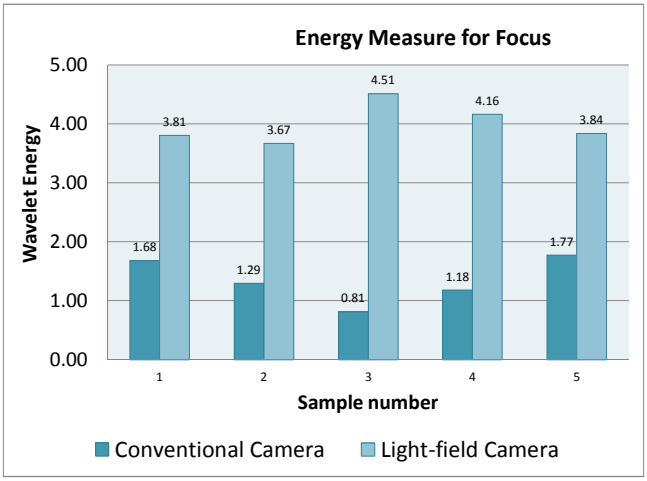

Fig. 5. Wavelet energy measured for best-focused iris images from light-field camera and conventional camera.

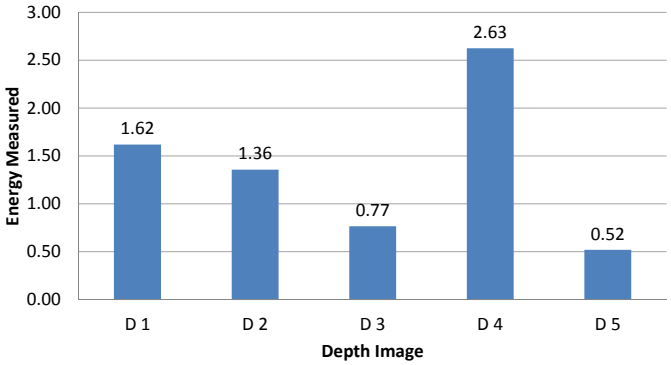

Fig. 6. Wavelet energy measured for multiple depth images for a single exposure acquisition.

III-C. Feature extraction and classification

Six well known feature extraction schemes [19], [20], [21], [22], [23], [24] have been employed in this work. Extracted features from the iris image are compared against the features obtained from the probe image. Hamming distance is used to measure the similarity of the iris images with 0 being a perfect match and 1 being a non-match.

IV. EXPERIMENTS AND RESULTS

The quantitative results of the experiments on our newly collected Iris dataset using both Light-field and conventional camera are discussed in this section. A total of 84 unique iris data obtained each from Light-field camera and conventional 2D camera were used in this work. The experiments were conducted using 420 iris images corresponding to conventional camera and 420 best focused images corresponding to light-field camera. 3387 depth images were used to measure the focus to obtain 420 best focused images. The whole set of iris images was evaluated for the identification accuracy

using the state-of-the-art iris recognition algorithms [19], [20], [21], [22], [23], [24].

The experiment resulted in 840 genuine comparisons and 87150 imposter comparisons. The results of the experiments are presented in terms of Equal Error Rate (EER) which is defined as the point where the False Match Rate (FMR) equals False Non-Match Rate (FNMR) [25]. Table I shows the quantitative performance in terms of EER (%) for light-field camera as compared to the conventional camera for various feature extraction schemes. It can be observed that the performance of the best-focus images obtained by the light-field camera exceeds by 4.64% on average as compared to the conventional camera and the best performance with lowest EER is noted for 2D Gabor based iris features [19].

Table I. Quantitative results obtained from various schemes

Feature Extraction	EER (%)	
	Light-field Camera	Conventional camera
Rathgeb & Uhl [21]	26.92	27.38
Rathgeb & Uhl [23]	11.84	18.24
Ko et al. [24]	5.95	12.55
Ma et al. [22]	5.78	12.07
Masek et al. [20]	5.26	12.44
Daugman [19]	2.38	8.53

Receiver operating characteristic (ROC) graphs for light-field camera and conventional camera are presented in Figure 7 and 8 respectively. The ROC shows the clear increase in $1 - FNMR$ at $FMR = 10^{-1}$ for the light-field camera in Figure 8. Thus from the results given in this section, it has been experimentally verified that the light-field camera provides much higher accuracy in the visible spectrum iris recognition.

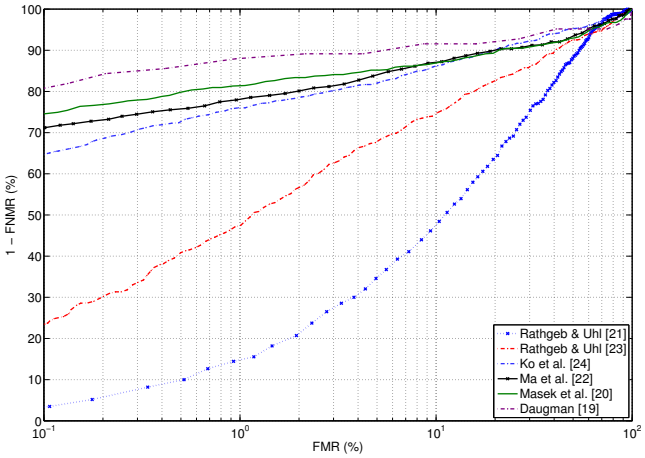

Fig. 7. Receiving Operator Characteristic graph for conventional iris images.

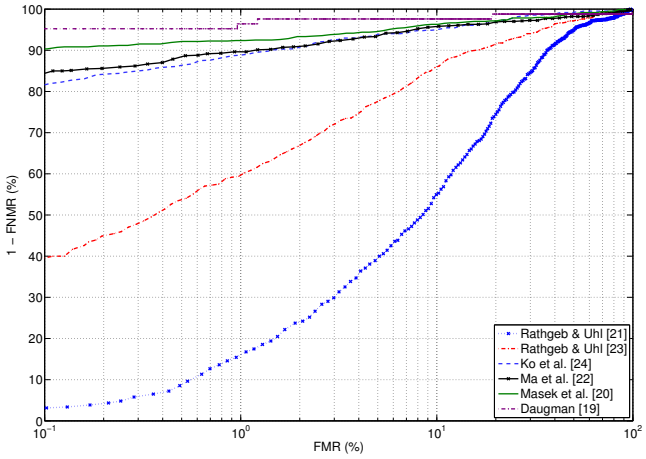

Fig. 8. Receiving Operator Characteristic graph for best-focused iris images from light-field camera.

V. CONCLUSIONS

The main motivation of this work is to address the out-of-focus images in the conventional iris imaging systems under visible spectrum. We have explored the strength of the light-field technology for the benefit of iris imaging. Multiple depth images obtained from single exposure are analyzed using the newly proposed energy based measure to obtain a best focused image. The best focused image is then employed for iris recognition to address the draw-backs of out-of-focus iris images. Due to limited depth-of-field in conventional cameras for iris imaging the acquisition of iris samples has to be repeated to obtain the best-focus. We have employed the Lytro light-field camera to experimentally validate our proposed scheme. The whole experiment was conducted on 84 unique irises with 5 samples for each iris captured using conventional camera and light-field camera. This work has resulted in the creation of a unique iris database captured with conventional camera and light-field camera with 420 sample images along with 3387 multiple-focus images. This light-field iris image database is the first and unique database to the best of our knowledge. The outcomes of the experiment have shown the success of the proposed scheme. The comparison of the performance of best-focused light-field iris images with conventional iris images has indicated better performance for the proposed scheme. Best-focused images obtained from the light-field camera reported an EER of 2.38% with 2D Gabor features proposed by Daugman [19] (refer to Table I), while the degraded performance has been demonstrated of 26.92% for the context based iris features [21]. The light-field images have given an average improvement of around 4.64% as compared to conventional images.

VI. ACKNOWLEDGMENT

This work was supported by the Erasmus Mundus Master CIMET and EU 7^{th} Framework Program (FP7/2007-2013) under grant agreement n^o 284862 for the large-scale integrated project FIDELITY.

VII. REFERENCES

[1] FH Adler, "Physiology of the eye, mosby, st," *Louis, Mo*, 1965.

[2] MR Chedekel, "Photophysics and photochemistry of melanin," *Melanin: Its Role in Human Photoprotection*, pp. 11–23, 1995.

[3] Yael Adini, Yael Moses, and Shimon Ullman, "Face recognition: The problem of compensating for changes in illumination direction," *Pattern Analysis and Machine Intelligence, IEEE Transactions on*, vol. 19, no. 7, pp. 721–732, 1997.

[4] Atos Origin, "Uk passport service biometrics enrolment trial," *Report. Retrieved April*, vol. 15, pp. 2009, 2005.

[5] Hugo Proença, "Iris recognition in the visible wavelength," in *Handbook of Iris Recognition*, pp. 151–169. Springer, 2013.

[6] Kevin W Bowyer, Karen Hollingsworth, and Patrick J Flynn, "Image understanding for iris biometrics: A survey," *Computer vision and image understanding*, vol. 110, no. 2, pp. 281–307, 2008.

[7] Nathan D Kalka, Jinyu Zuo, Natalia A Schmid, and Bojan Cukic, "Estimating and fusing quality factors for iris biometric images," *Systems, Man and Cybernetics, Part A: Systems and Humans, IEEE Transactions on*, vol. 40, no. 3, pp. 509–524, 2010.

[8] Ramkumar Narayanswamy, Paulo EX Silveira, Harsha Setty, V Paul Pauca, and Joseph van der Gracht, "Extended depth-of-field iris recognition system for a workstation environment," in *Defense and Security*. International Society for Optics and Photonics, 2005, pp. 41–50.

[9] Naresh Boddeti and BVKV Kumar, "Extended depth of field iris recognition with correlation filters," in *Biometrics: Theory, Applications and Systems, 2008. BTAS 2008. 2nd IEEE International Conference on*. IEEE, 2008, pp. 1–8.

[10] Kang Ryoung Park and Jaihie Kim, "A real-time focusing algorithm for iris recognition camera," *Systems, Man, and Cybernetics, Part C: Applications and Reviews, IEEE Transactions on*, vol. 35, no. 3, pp. 441–444, 2005.

[11] Sriram Pavan Tankasala, Vikas Gottemukkula, Sashi Kanth Saripalle, Venkata Goutam Nalamati, Reza Derakhshani, Raghunandan Pasula, and Arun Ross, "A video-based hyper-focal imaging method for iris recognition in the visible spectrum," in *Homeland Security (HST), 2012 IEEE Conference on Technologies for*. IEEE, 2012, pp. 214–219.

[12] Lytro Inc, ," http://www.lytro.com/.

[13] Ren Ng, Marc Levoy, Mathieu Brédif, Gene Duval, Mark Horowitz, and Pat Hanrahan, "Light field photography with a hand-held plenoptic camera," *Computer Science Technical Report CSTR*, vol. 2, 2005.

[14] Ashok Veeraraghavan, Ramesh Raskar, Amit Agrawal, Ankit Mohan, and Jack Tumblin, "Dappled photography: Mask enhanced cameras for heterodyned light fields and coded aperture refocusing," *ACM Transactions on Graphics*, vol. 26, no. 3, pp. 69, 2007.

[15] R. Raghavendra, Bian Yang, Kiran B. Raja, and Christoph Busch, "A new perspective - face recognition with light-field camera," in *6th IAPR International Conference on Biometrics (ICB), Madrid*. IEEE, 2013.

[16] Nobuyuki Otsu, "A threshold selection method from gray-level histograms," *Automatica*, vol. 11, no. 285-296, pp. 23–27, 1975.

[17] Guillaume Sutra, Bernadette Dorizzi, Sonia Garcia-Salicetti, and Nadia Othman, "A biometric reference system for iris, osiris version 4.1," 2012.

[18] Thierry Lefevre, Bernadette Dorizzi, Sonia Garcia-Salicetti, Nadege Lemperiere, and Stephane Belardi, "Effective elliptic fitting for iris normalization," *Computer Vision and Image Understanding*, 2013.

[19] John Daugman, "How iris recognition works," in *Image Processing. 2002. Proceedings. 2002 International Conference on*. IEEE, 2002, vol. 1, pp. I–33.

[20] Libor Masek, "Recognition of human iris patterns for biometric identification," M.S. thesis, University of Western Australia, 2003.

[21] Christian Rathgeb and Andreas Uhl, "Context-based texture analysis for secure revocable iris-biometric key generation," in *Crime Detection and Prevention (ICDP 2009), 3rd International Conference on*. IET, 2009, pp. 1–6.

[22] Li Ma, Tieniu Tan, Yunhong Wang, and Dexin Zhang, "Personal identification based on iris texture analysis," *Pattern Analysis and Machine Intelligence, IEEE Transactions on*, vol. 25, no. 12, pp. 1519–1533, 2003.

[23] Christian Rathgeb and Andreas Uhl, "Secure iris recognition based on local intensity variations," in *Image Analysis and Recognition*, pp. 266–275. Springer, 2010.

[24] Jong-Gook Ko, Youn-Hee Gil, Jang-Hee Yoo, and Kyo-IL Chung, "A novel and efficient feature extraction method for iris recognition," *ETRI journal*, vol. 29, no. 3, pp. 399–401, 2007.

[25] ISO/IEC TC JTC1 SC37 Biometrics, *ISO/IEC 19795-1:2006. Information Technology – Biometric Performance Testing and Reporting – Part 1: Principles and Framework*, International Organization for Standardization and International Electrotechnical Committee, Mar. 2006.